SAND--96-8497C
CONF-960204--8
960831

OH Radical Imaging in a DI Diesel Engine and the Structure of the Early Diffusion Flame*

John E. Dec and Edward B. Coy
Sandia National Laboratories

ABSTRACT

Laser-sheet imaging studies have considerably advanced our understanding of diesel combustion; however, the location and nature of the flame zones within the combusting fuel jet have been largely unstudied. To address this issue, planar laser-induced fluorescence (PLIF) imaging of the OH radical has been applied to the reacting fuel jet of a direct-injection diesel engine of the "heavy-duty" size class, modified for optical access. An Nd:YAG-based laser system was used to pump the overlapping $Q_1 9$ and $Q_2 8$ lines of the (1,0) band of the A→X transition at 284.01 nm, while the fluorescent emission from both the (0,0) and (1,1) bands (308 to 320 nm) was imaged with an intensified video camera. This scheme allowed rejection of elastically scattered laser light, PAH fluorescence, and laser-induced incandescence.

OH PLIF is shown to be an excellent diagnostic for diesel diffusion flames. The signal is strong, and it is confined to a narrow region about the flame front because the three-body recombination reactions that reduce high flame-front OH concentrations to equilibrium levels occur rapidly at diesel pressures. No signal was evident in the fuel-rich premixed flame regions where calculations and burner experiments indicate that OH concentrations will be below detectable limits. Temporal sequences of OH PLIF images are presented showing the onset and development of the early diffusion flame up to the time that soot obscures the images. These images show that the diffusion flame develops around the periphery of the downstream portion of the reacting fuel jet about half way through the premixed burn spike. Although affected by turbulence, the diffusion flame remains at the jet periphery for the rest of the imaged sequence. The images also show many details of the diffusion flame structure including its upstream extent. Finally, the location and nature of the diffusion flames are discussed with respect to previously reported soot and fuel distributions.

* This work was performed at the Combustion Research Facility, Sandia National Laboratories and was supported by the Cummins Engine Co. and the U.S. Dept. of Energy, Defense Programs Technology Transfer Initiative.

INTRODUCTION

The location and nature of the reaction zones are among the most fundamental aspects of diesel combustion, yet they have been largely uninvestigated. Knowledge of these reaction zones is central to improving our understanding of diesel combustion and the associated production of emissions. In addition, this information is critical for the development of truly predictive computer models and for guiding the design of future diesel engines that must have both higher efficiencies and lower emissions.

Diesel combustion contains both premixed and diffusion reaction zones. Initially, a premixed burn occurs because some fuel and air have mixed prior to autoignition. Following this is the mixing-controlled burn which is thought to be dominated by diffusion combustion, but may contain premixed combustion as well. Recent studies [1,2] have shown that the initial premixed burn is fuel rich (equivalence ratios of 2 to 4), and that the later premixed combustion is also likely to be fuel rich, since all the fuel is fully vaporized and premixed to an equivalence ratio in the neighborhood of 4 prior to entering the main reaction zone. Other than this information on fuel/air mixtures, little is known about diesel reaction zones. Previous studies have allowed inferences to be made about the location and timing of these reaction zones, but to date there is little definitive data.

Planar laser-induced fluorescence (PLIF) imaging of the combustion radicals provides a means of studying the diesel reaction zones. Both the CH [3-7] and OH [3-5,8-10] radicals have been used in burner experiments to visualize the reaction zones in hydrocarbon flames. Although the CH radical is generally a better marker of the reaction zone [3-7], PLIF of CH can be difficult due to weak signals and the required laser characteristics (wavelength and pulse duration) [7]. Recently, Paul and Dec [7] demonstrated a new technique for CH PLIF that offered several improvements over traditional CH techniques. However, we applied this technique to the diesel engine and found that signals were too weak and interferences from PAH (poly-aromatic hydrocarbon) fluorescence and LII (laser-induced incandescence) were too great to make useful measurements. In contrast, OH PLIF typically has a

much stronger signal, the laser system is straightforward [8], and although PAH and LII interferences are still a concern for diesel applications, they can be adequately removed by spectral filtering.

Because of these advantages, PLIF imaging of the OH radical has been widely applied to the study of both premixed [3,8,9] and diffusion [4,5,10] flames in burners. These imaging studies and other burner studies (using both absorption and point laser-induced fluorescence) [11-16] have shown that the OH radical distribution is initiated in the flame front and almost immediately rises to high (super-equilibrium) concentrations that are on the order of 3 to 5 times flame-zone equilibrium levels [5,11,13]. In the post-combustion gases, the OH concentration gradually drops off to the local equilibrium value by a three-body recombination reaction [13] whose rate is strongly dependent on pressure. This rate is slow at atmospheric pressure, and OH often persists well away from the flame front making it a less useful marker of the reaction zone [3,5,10,13]. However, as ambient pressure is increased, the super-equilibrium OH concentrations in the flame zone are more rapidly reduced to the equilibrium levels outside the flame zone [12,17]. Furthermore, for diffusion flames, the equilibrium level itself falls rapidly outside of the flame zone [13]. The combination of these two effects causes the OH concentration (and hence OH PLIF signal) to closely mark the reaction zone in high-pressure diffusion flames, with a large signal differential from the flame zone to the surrounding gas. This has recently been demonstrated by Allen et al. [17] who found the OH signal from the diffusion-flame zone of a steady spray flame to become progressively thinner as pressure was increased from 1 to 9.5 bar. At diesel conditions, where pressures are 50 bar or higher, the effect should be even more dramatic, and OH PLIF is expected to closely mark the diffusion flame zones.

Another effect that would cause the OH distribution to be more localized about the flame zone is the removal of OH by soot oxidation. Burner studies have shown that OH is important in soot oxidation, and conversely they indicated that the presence of soot and soot precursors can decrease OH concentrations [14-16]. Puri et al. [16] demonstrated this effect by measuring the OH concentrations in a simple diffusion flame for three different fuels that produced increasing amounts of soot and related hydrocarbons. For the lowest sooting fuel (methane), they found OH persisting far from the flame zone on the fuel side of the diffusion flame. As other species (butane and butene) were added to the methane, progressively more soot was produced, and the OH concentration fell off at progressively higher rates on the fuel side of the diffusion flame. For diesel combustion, this effect would cause the OH distribution to be more localized about the flame zone similar to the three-body mechanism, but its effect would be limited to the fuel-rich side of the diffusion flame.

Finally, the burner studies indicate that PLIF of OH will provide a good image of the diffusion flame but may not be capable of detecting the premixed combustion in diesel engines, which recent measurements have shown occurs at equivalence ratios in the range of 2 to 4 [1,2] for the typical operating condition examined. OH concentrations in diffusion flames and in lean and near-stiochiometric premixed flames are relatively high with peak concentrations ranging from about 0.6×10^{16} - 2.0×10^{16}/cm^3 [5,11,16,18]. These concentrations give strong PLIF signals and are easily imaged. However, for fuel-rich premixed flames Lucht et al. [11] found both peak and near-equilibrium OH concentrations to be much lower. Also, as they increased the equivalence ratio in the rich flame, OH concentrations continued to drop, with both peak and post-combustion gas values being about 100 times less for an equivalence ratio of 2.02 than those for an equivalence ratio of 0.78. Thus, the fuel-rich premixed combustion in a diesel engine (equivalence ratios of 2 to 4), will likely have OH concentrations that are below the detectability limits of OH PLIF.

OH PLIF has also been demonstrated as a technique for studying flames in internal combustion engines. For the most part, these previous works have involved using OH PLIF to visualize the flame fronts in spark ignition engines [19-21]. In these premixed-charge engines, the images showed the OH distribution beginning at the flame front and persisting into the post-combustion gases. There has also been one previous attempt to obtain OH PLIF images in a diesel engine [22]. However, the study was limited in scope, and it involved a small-bore diesel engine with limited optical access. A fairly narrow laser sheet was used to illuminate a path across the combustion bowl and images are presented at only one crank angle. Some signal was produced, but it was not obtained or reported in such a way that it can be related to the physics and chemistry of the diesel combustion process.

The objective of the current study is to use OH PLIF to investigate the turbulent diffusion flame structure of a reacting diesel fuel jet in a direct-injection (DI) diesel engine. Using a diesel engine of the heavy-duty size class modified for optical access, OH PLIF images have been acquired from just after the start of combustion up through the development of the early diffusion flame. Images were obtained both in a plane along the fuel-jet axis and in multiple horizontal planes to more fully reveal the flame structure. These OH distribution images show the inception and primary development of the turbulent diffusion flame. In some images, optical filters are selected that allow Mie scattering from the liquid phase fuel to be imaged along with the OH fluorescence. Since the two signals are spatially separated, these images show the position of the upstream edge of the diffusion flame relative to the liquid-phase fuel. In addition, the timing and structure of the diffusion flame as shown by these OH images is related to the our recent work which mapped out the ignition and early soot-formation processes in this engine [23].

Following this introduction, the experimental setup is described, including the optically accessible engine, operating conditions, apparent heat release rate curves, and the optical setup for OH PLIF. Then, signal-to-noise issues in OH PLIF imaging and the selection of optical filters are discussed. Next, the results and discussion are presented in four parts. The first three parts present and discuss temporal and spatial sequences of OH PLIF images of the reacting diesel fuel jet. In the fourth part, the diffusion flame structure as determined from these OH data is discussed and related to previous stud-

ies of early combustion and soot formation processes. In the final section, the findings are summarized and conclusions drawn.

EXPERIMENT DESCRIPTION

OPTICAL-ACCESS ENGINE

The optical-access engine used in this study was a single-cylinder, direct-injection, 4-stroke diesel engine based on a Cummins N-series production engine. The N-series engine is typical of heavy-duty size-class diesel engines, with a bore of 140 mm and a stroke of 152 mm. These dimensions are retained in the optical-access engine, and a production Cummins N-series cylinder head is used so that the production engine intake port geometry is also preserved. The in-cylinder flow field of a similar Cummins N-series research engine has been examined under motored conditions and found to be nearly quiescent [24]. Figure 1 presents a schematic of the engine, and Table 1 summarizes its specifications.

TABLE 1. Specifications of the Optical-Access Engine

Engine base type	Cummins N-14, DI Diesel
Number of cylinders	1
Cycle	4-stroke
Number of intake valves	2
Number of exhaust valves	1[a]
Combustion chamber	Quiescent, direct injection
Bore	139.7 mm (5.5 in)
Stroke	152.4 mm (6.0 in)
Combustion chamber diameter	97.8 mm (3.85 in)
Displacement	2.34 liters (142 in^3)
Connecting rod length	304.8 mm (12.0 in)
Piston pin offset	None
Compression ratio	10:1

[a] In this optically accessible Diesel engine, one of the two exhaust valves of the production cylinder head was replaced by a window and periscope.

The design of this engine utilizes a classic extended piston with piston-crown window. Additional windows located around the top of the cylinder wall provide the orthogonal optical access required for the two-dimensional (planar) laser imaging diagnostics. These windows allow the laser sheet to enter the cylinder along the axis of the fuel jet (see Fig 1) or horizontally. A window in the cylinder head replaces one of the two exhaust valves to obtain a view of the squish region and the outer portion of the combustion bowl. Finally, but perhaps most important for studies of the diesel fuel jet, this optical access engine incorporates a unique separating cylinder liner to allow rapid cleaning of the windows. A complete description of this engine may be found in Ref. [25].

This research engine is equipped with the Cummins CELECT electronic fuel injector. This closed-nozzle unit injector uses camshaft actuation to build injection pressures. A solenoid valve in the injector body controls the amount of fuel injected and the injection timing upon command from the laboratory computer. For the experiments presented here, the injector was equipped with an 8-hole cup. The hole diameter was 0.194 mm and the nominal angle of the fuel-jet axis was 14° downward from horizontal. Table 2 summarizes the specifications of the fuel injector. The injector is instrumented with a Hall-effect needle lift sensor, and injection pressure is determined from strain gage measurements of the force in the pushtube that activates the injector. Injection pressures and needle-lift data presented are typical of those of N-series production engines using this injector at the operating conditions studied.

To minimize vibration, the engine was connected to a balancing box with counter-rotating balancing weights and mounted on a spring-mounted isolation pad. The engine was motored and its speed controlled by a 75 hp dynamometer.

TABLE 2. Specifications of the Fuel Injector

Type	Cummins CELECT™
Design	Closed-nozzle, unit injector
Number of holes	8, uniformly spaced
Hole diameter	0.194 mm
Length/diameter of holes (l/d)	4.1
Angle of fuel-jet axis (from horizontal)	14°

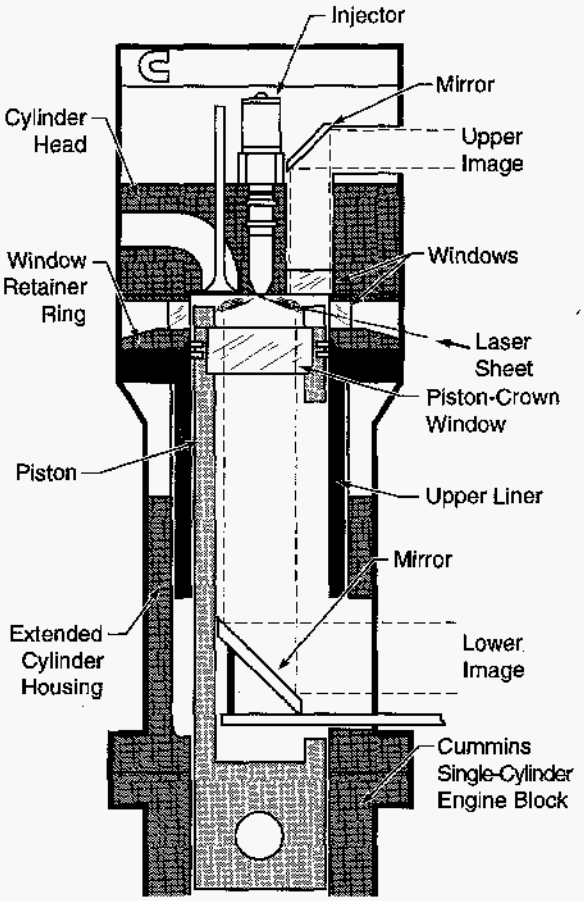

Figure 1. Schematic of optical-access Diesel engine showing the laser sheet along the fuel jet axis. Images were obtained through both the cylinder-head window (upper image) and the piston-crown window (lower image). The upper liner is shown in the operating position.

An air compressor supplied pressurized intake air that was dehumidified and heated.

To minimize interfering signals from dirt particles and compressor oil special care was taken with the engine air and fuel supply systems. The intake-air-supply compressor was fitted with an intake filter and oil-droplet/air separator. In addition, the air passed through another two-stage filter system after it was dehumidified. The first stage contained a 0.01 μm filter to remove small particulate matter, and the second stage was an activated-charcoal filter to both remove any remaining compressor oil vapor. Fuel was supplied by a stainless steel diaphragm pump to avoid the contamination from small particles that can result from a gear-type pump.

OPERATING CONDITIONS

All the data presented in this article were taken at an engine speed of 1200 rpm. Before conducting the experiments the engine was heated to 368 K (95° C) by means of electrical heaters on the "cooling" water and lubricating oil circulation systems. To minimize the rate of window fouling and to avoid overheating, the engine was fired once every 10th engine cycle, at which time the data were acquired.

Measurements were made at an operating condition that is representative of Diesel engine conditions. Because the optical-access engine has a compression ratio of only 10:1, intake air temperatures and pressures were increased so that motored TDC (top dead center) conditions were representative of typical Diesel engine conditions. For the base condition, the intake air was heated to 433 K (160° C) to obtain a realistic ignition delay and premixed burn fraction. The intake pressure was set to 206 kPa absolute to match the TDC air density of a naturally aspirated engine with the 16:1 compression ratio of a production Cummins N-series engine. This resulted in a TDC pressure of 5.0 MPa and an estimated TDC temperature of 992 K, for the motored engine assuming a polytropic coefficient of 1.36. The operating conditions are summarized in Table 3.

With the fuel injector used, changing the amount of fuel injected (at an otherwise fixed operating condition) changes only the injection duration and not the initial injection rate. Since the current study is concerned only with events up through the first part of combustion, a relatively low fuel load (average equivalence ratio of 0.25) was used to minimize window fouling.

TABLE 3. Base Engine Operating Conditions

Engine speed	1200 rpm
Intake air temperature	433 K (160° C)
Intake air pressure	206 kPa (absolute)
Water temperature	95° C
Oil temperature	95° C
Firing rate	Every 10th cycle
Start of injection	11.5° BTDC
Average equivalence ratio	0.25
Peak injection pressure	68 MPa
Motored TDC pressure	5.0 MPa
Estimated motored TDC temperature	992 K
Estimated motored TDC density	16.6 kg/m^3

PLIF of OH requires both the laser and the fluorescence signal to be at ultraviolet wavelengths that are easily attenuated by both PAH and soot in the combusting fuel jet. To minimize these effects, low-sooting fuel mixtures were used. For most of the data, a mixture of 70% tetraethoxypropane and 30% heptamethylnonane (by volume) was used. This fuel, which will be referred to as the low-sooting fuel, is the same one used to minimize optical attenuation in our previous investigations of the early stages of diesel combustion [23].* The apparent ignition delay and the behavior of the early combustion and soot formation processes for this fuel have been examined in great detail and found to be virtually identical to those of a 42.5 cetane-number mixture of the reference fuels (heptamethylnonane and *n*-hexadecane), with the exception of lower soot concentrations [23]. In addition, the boiling points of the low-sooting fuel constituents are near those of the diesel reference fuels and near those of some representative diesel fuel constituents. Accordingly, we believe that the OH measurements presented in this article are representative of diesel combustion with realistic fuels.

In addition to the low-sooting fuel, a few measurements were made using 100% tetraethoxypropane as a fuel. This fuel, which will be referred to as pure TEOP, was used because it produces even less attenuation than the low-sooting fuel; however, it has a shorter ignition delay. We estimate the cetane number of pure TEOP to be 54 from volume fraction calculations of the low-sooting fuel. The shorter ignition delay of this fuel is in agreement with the estimated cetane number.

A complete discussion of the low-sooting fuel, a comparison with the equivalent reference fuel, and a discussion of the assumptions involved in using a low-sooting fuel may be found in Ref. [23]. Table 4 gives the properties of the two fuels used and the amount of fuel injected per cycle. The diesel reference fuel mixture used in Ref. [23] is also given for comparison.

TABLE 4. Fuels

Low-Sooting Fuel	**70% tetraethoxypropane and 30% heptamethylnonane**
Estimated Cetane No.	42.5
Specific Gravity	0.88
Fuel Injected per Cycle	0.0960 ml
Pure TEOP Fuel	**100% tetraethoxypropane**
Estimated Cetane No.	54
Specific Gravity	0.92
Fuel Injected per Cycle	0.0960 ml
Reference Fuel (used in Ref. [23] - for comparison)	**67.6% heptamethylnonane and 32.4% *n*-hexadecane**
Cetane No.	42.5
Specific Gravity	0.79
Fuel Injected per Cycle	0.0858 ml
Boiling Points of Constituents (1 Atm.)	
2,2,4,4,6,8,8 Heptamethylnonane	240° C
n-Hexadecane	287° C
1,1,3,3 Tetraethoxypropane	220° C

* Even for visible wavelengths, the diesel plume has been found to be optically thick when typical diesel fuels are used as reported by the first author and co-workers [23,25,26] and others [27,28].

APPARENT HEAT RELEASE RATES

For both fuels the cylinder pressure, fuel injection pressure, and injector needle lift data were digitized and recorded at half crank-angle-degree increments and ensemble-averaged over 20 engine cycles. The apparent heat release rate was calculated from the ensemble-averaged cylinder pressure data using the typical first law and perfect gas analysis (see for example Heywood [29]). Prior to calculating the apparent heat release rate, the ensemble-averaged pressure data were smoothed with a Fourier series high-frequency-reject filtering algorithm that used a Gaussian roll-off function as discussed in an earlier paper [30].

Figures 2 and 3 present plots of the apparent heat release rate, cylinder pressure, and injector needle lift for the low-sooting and pure TEOP fuels, respectively. In these figures, the plot of the needle lift indicates that injection begins at about 11.5° before top dead center (-11.5° after top dead center, ATDC). Because the time after the start of injection is the relevant parameter for the fuel-jet development, all discussions in the remainder of this article will be given in crank angle degrees after the start of injection (ASI).

As is typically found in diesel combustion, the apparent heat release rate curves in Figs. 2 and 3 first go negative just after the start of injection as fuel vaporization cools the in-cylinder air. Then, after a few degrees, the combustion energy release exceeds that required for vaporizing the fuel, and the apparent heat release rises rapidly. Although the authors have shown by chemiluminescence imaging [23] that "ignition" actually begins prior to this rapid rise in the apparent heat release rate curve, the onset of the rapid rise provides a convenient repeatable point for comparing various data sets. This point, which will be referred to as the first indicated heat release, occurs at 4.0° ASI (-7.5° ATDC) for the low-sooting fuel,* as indicated by the edge of the light gray shaded area in Fig. 2. This first indicated heat release occurs at about 2.5° ASI (-9.0° ATDC) for the pure TEOP fuel, which has a higher cetane number. Accordingly, the apparent ignition delay (the time from the first indication of injector needle lift to the point of the first indicated heat release) is 4° (556 μs) for the low-sooting fuel and 2.5° (347 μs) for the pure TEOP.

After the ignition delay, the apparent heat release rises rapidly through the premixed burn spike then drops sharply before rising again more slowly through the mixing-controlled portion of the combustion event. The pure TEOP fuel has less time for premixing of the fuel and air due to its shorter ignition delay, resulting in a smaller premixed burn spike.

OPTICAL SETUP AND IMAGE ACQUISITION

The OH fluorescence was excited by pumping the overlapping $Q_1 9$ and $Q_2 8$ lines of the (1,0) band of the A→X transition at 284.01 nm [31]. This line was selected for its high fluorescence yield and because it is relatively insensitive to temperature variations. Fluorescent emission was collected from both the (0,0) and (1,1) bands in the 308 to 320 nm range [31]. This fluorescence scheme provided a strong signal and allowed rejection of the elastically scattered light. The latter feature is an important consideration for PLIF in diesel engines since soot, liquid fuel, windows and walls can all create strong elastic-scatter signals. This fluorescence scheme also allowed rejection of the interfering signals from PAH fluorescence and LII that occur mainly above about 330 nm.

An Nd:YAG-pumped dye laser (PDL-3 with rhodamine 590 dye) and frequency doubling crystal were used to create the 284 nm pump beam. A combination of cylindrical and spherical lenses was used to convert the laser beam into the sheet required for PLIF imaging. This produced a light sheet approximately 250 μm thick and 25 mm wide in the imaged region of the fuel jet. Laser energies prior to entering the cylinder were about 24 mJ per pulse.

For this study images were acquired both with a horizontal laser sheet and with the laser sheet on the fuel jet axis as shown in Fig. 4. The sheet-forming optics produced a horizontal laser sheet, and a motorized drive translating stage allowed the horizontal laser sheet to be adjusted vertically to obtain images at various elevations. For the on-axis images, a pair of mirrors was used to aim the laser sheet at an angle of 14° upward from horizontal so that it approached the fuel jet along its axis. The laser sheet was directed into the combustion chamber through one of the windows at the top of the cylinder wall which was in line with one of the fuel jets. The piston bowl rim was cut out in line with the laser sheet to permit the laser sheet to enter the combustion chamber near TDC (Fig. 4).

Images were acquired through both the piston-crown and cylinder-head windows with a gated, intensified CCD video camera. A 105 mm Nikkor f/4.5 UV lens was used for all images. As discussed in the next section, various filters were placed in front of the camera lens to isolate the PLIF signal from the elastically scattered laser light and the background PAH and LII emission. The image intensifier on the camera has been calibrated [2] so that the intensities of images taken at different intensifier gain settings could be compared. The intensifier gatewidth was set to 70 ns and the camera intensifier gate was synchronized with the 7 ns laser pulse. The camera had a video chip resolution of 380 by 480 pixels and was digitized by an 8-bit frame grabber in a 386 personal computer to a resolution of 512 by 480 pixels.

Synchronization between the engine, laser, camera, and intensifier gate was controlled by a second personal computer and a digital delay generator, with the master signal coming from the engine shaft encoder. The camera was equipped with a frame-transfer inhibit feature that allowed the video frame acquisition to be synchronized with the engine. This synchronization system could be adjusted to obtain images at any desired crank angle within the half-degree resolution of the shaft encoder. Although each image has an effective exposure time of only about 7 ns, only one image could be acquired in a given cycle due to speed limitations of the laser

* In Ref. [23], a different filtering algorithm was used to reduce the cylinder pressure data to apparent heat release rate. This caused some small differences in the apparent heat release rate curve and the first indicated heat release was taken to be 4.5° ASI (-7.0° ATDC).

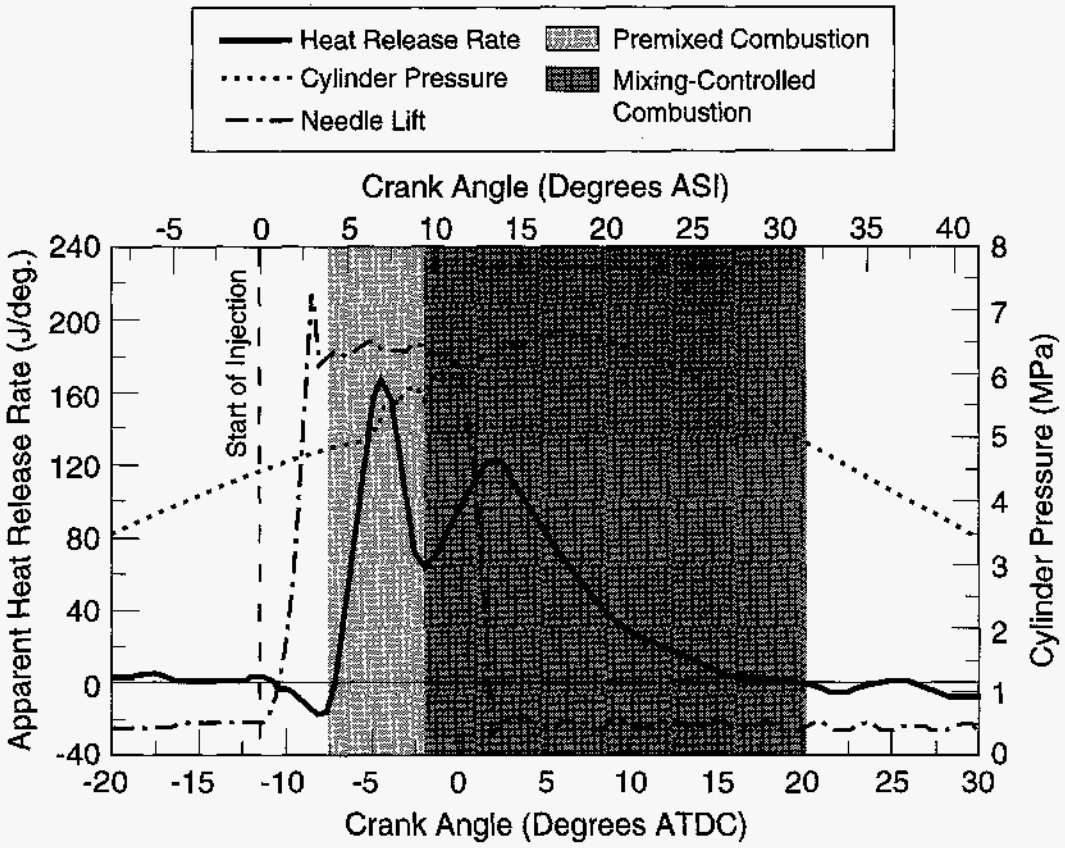

Figure 2. Heat release rate, cylinder pressure, and injector needle lift for the low-sooting fuel. Data are ensemble-averaged over 20 cycles.

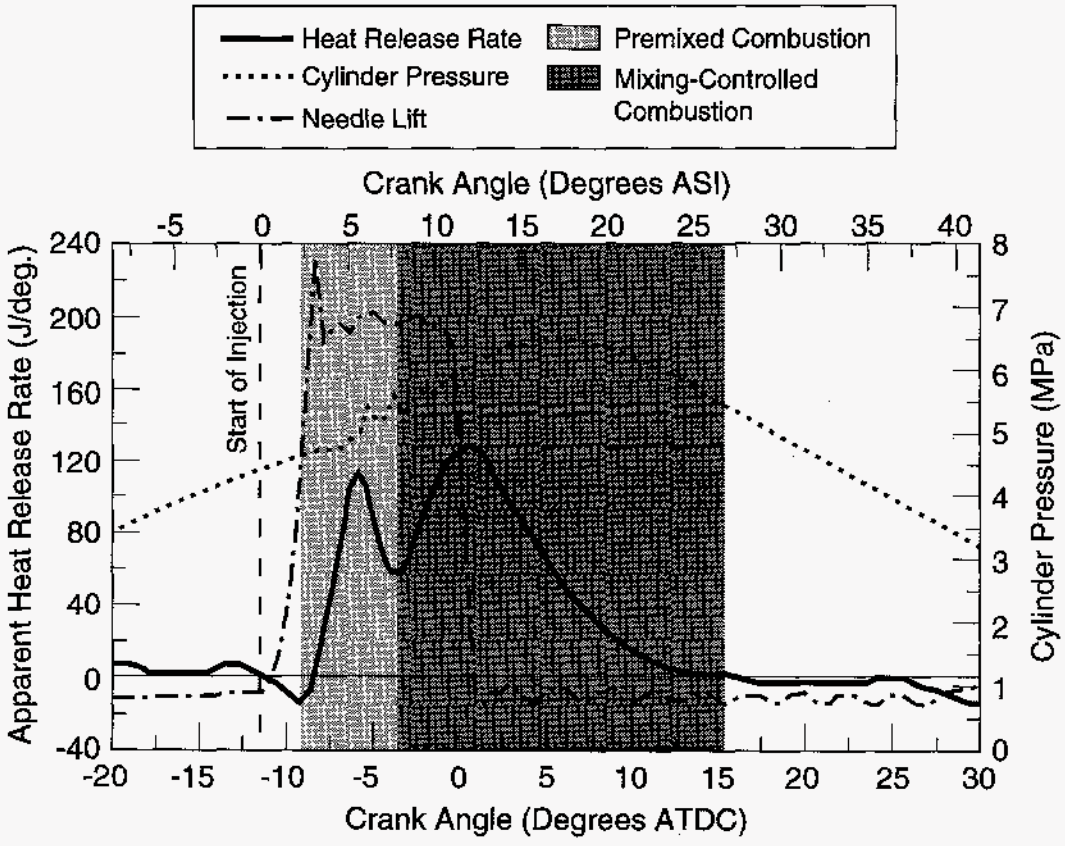

Figure 3. Heat release rate, cylinder pressure, and injector needle lift for the pure TEOP. Data are ensemble-averaged over 20 cycles.

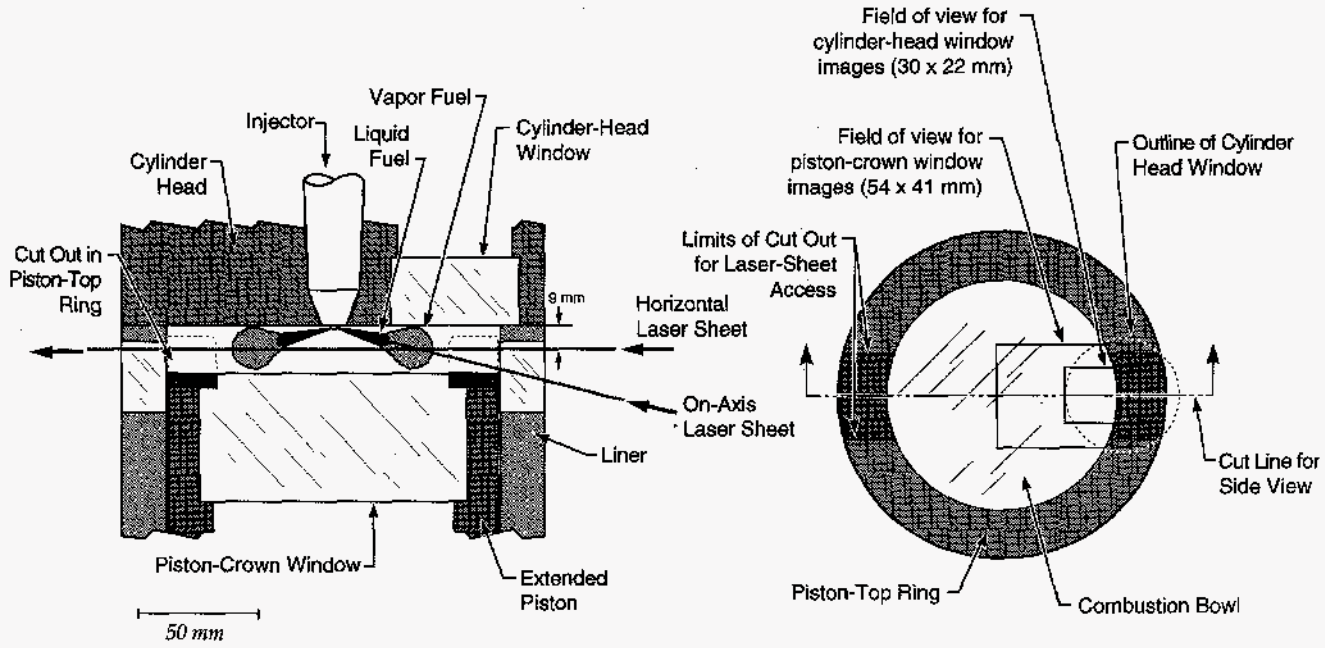

Side View of Combustion Chamber **Top View of Piston**

Figure 4. Geometry and optical configuration of the combustion chamber with cut outs in the rim for laser access. Figure 4a shows a side view of the combustion chamber and the two laser-sheet orientations. Figure 4b shows the top view of the piston and the field of view for images obtained through both piston-crown and the cylinder-head windows. The piston is shown at the TDC position.

and video recording system. Images were acquired in sets of 12 or 24, from 12 or 24 separate cycles. Each image presented has been subjectively selected as being representative of its respective set. We believe that the selected images represent typical OH distributions for their respective crank angles, and as such, they can be compared with the corresponding ensemble-averaged plots of the apparent heat release rate, cylinder pressure, and needle lift.

OH PLIF IMAGING FILTER SELECTION

There are two main noise sources in OH PLIF images in sooting environments such as diesel combustion: 1) elastically scattered laser light and 2) the broadband emission from PAH fluorescence and LII of the soot. As discussed in the previous section, the OH PLIF images were created by exciting the (1,0) band of the A→X transition at 284.01 nm and collecting the fluorescent emission in from the (0,0) and (1,1) bands in the 308 - 320 nm range (band peaks are at about 309 and 315 nm, respectively [31]). This spectral separation allows the elastically laser light to be rejected from the OH images with a long-wave-pass (LWP) filter.

The broadband emission is more difficult to remove. Fluorescence from PAHs is fairly easily excited by most UV wavelengths, including the 284 nm OH pump beam. The Stokes-shifted fluorescence is typically very broadband, extending from wavelengths somewhat longer than that of the laser up well into the visible. A typical example of a PAH is Pyrene which, when excited at 313 nm, fluoresces from about 360 to 530 nm with a peak emission at about 390 nm [32]. As illustrated by this example, for excitation at wavelengths near that used for OH, the majority of PAH emission is more red-shifted than the OH emission of interest. LII from the soot is a gray-body emission that is a function of the laser-heated soot temperature. The maximum soot temperature is limited by soot vaporization to about 4500 K [26]. An examination of the black-body emission curve shows that for this temperature, the radiant emission drops off significantly toward the UV, being relatively weak below 320 nm. Accordingly, a short-wave-pass (SWP) filter can be used to suppress both PAH and LII emission.

Unfortunately, the ideal filter for OH PLIF (one that has high transmission from 308 to 320 nm and good rejection of both the laser line and wavelengths longer than 320 nm) is not readily available. We examined three off-the-shelf filter combinations, found them unacceptable, and ordered a custom filter set.

A comparison of the four filter combinations is given in Fig. 5. For each filter combination, this figure shows OH images obtained through the cylinder-head window at 6.5° ASI with the laser tuned both on (284.01 nm) and off the OH absorption line (283.90 nm). As shown in Fig. 4, the left edge of the field of view is about 27 mm from the injector, so these images show only the leading portion of the reacting fuel jet. The effectiveness of each filter combination in removing background emission can be assessed by comparing the on- and off-line images. The number in the upper right of each image indicates the gain of the camera intensifier normalized by the gain of the images obtained with the custom filter set. First, a combination of a WG305 and a UG11 Schott glass filter was tried since it gives good transmission (70%) over

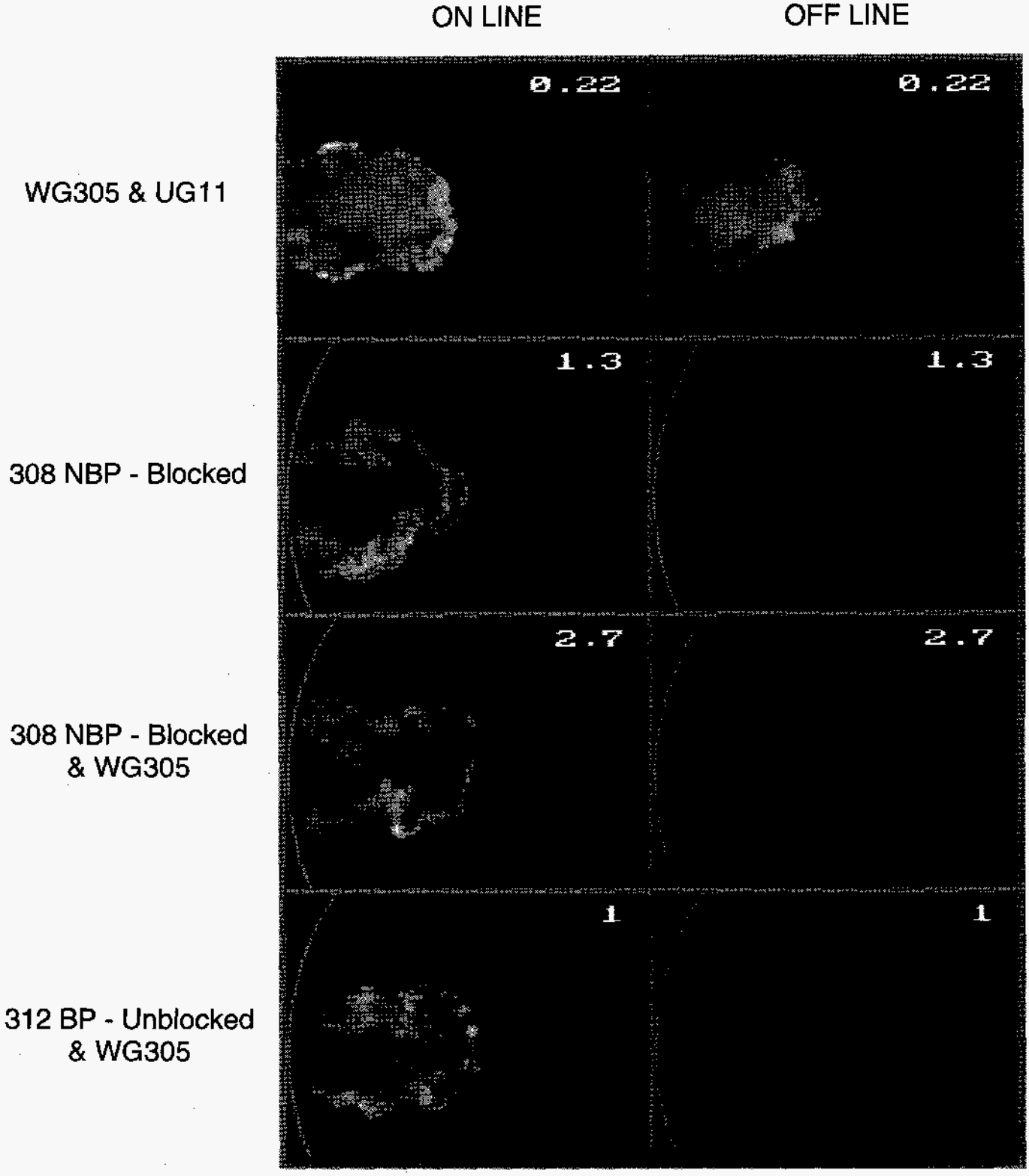

Figure 5. The effect of various filter combinations on the OH PLIF images obtained through the cylinder-head window at 6.5° ASI. On and off-line images are shown for each filter combination. The rectangular field of view is 30 mm by 22 mm, and the number at the upper right of each image indicates the camera gain relative to that used for the custom filter set. All on- and off-line sets were taken with the low-sooting fuel and the laser sheet on the fuel jet axis, except the top set (WG305 & UG11) which was taken using pure TEOP fuel with a horizontal laser sheet in the 9 mm plane. The gray curve at the left of the images for the last three filter sets indicates the limit of the field of view through this window (see Fig. 4).

the OH emission bands. The WG305 LWP filter effectively eliminates elastically scattered light, but the UG11 (which is acting as a 400 nm SWP filter in this application) allows significant broadband PAH/LII emission making image interpretation difficult. Second, a blocked 308 nm narrow-bandpass (NBP) filter (10 nm FWHM) was tried.* This filter eliminated most of the broadband PAH/LII emission, but significantly reduced the OH signal due to its narrow bandwidth and low (15%) peak transmission. Also, the off-line image in Fig. 5 shows a weak background signal coming from the jet and the edge of the piston bowl is faintly visible. Third, adding a WG305 LWP filter to the blocked 308 nm NBP filter suppresses the remaining background signal (indicating that it was from elastic scattering), but signal levels are relatively weak. Fourth, the custom filter set, consisting of an unblocked 312 nm bandpass (BP) interference filter** (16 nm FWHM) and a 358 nm SWP filter, provides good signal strength and adequately suppresses off-line emission. Peak transmission is about 50% and the 16 nm bandwidth allows almost all of the (0,0) and (1,1) bands to be collected. The unblocked 312 nm BP interference filter provides good light rejection from about 278 to 295 nm and from 330 to 350 nm then begins to transmit again at more extreme wavelengths. Accordingly, the laser line is well rejected as are most of the emissions between the OH line and the 358 SWP filter. Some PAH and LII emission between 350 and 358 nm is not fully suppressed, but this is a fairly narrow region where these noise emissions are not strong, and transmission still averages less than 10%.

The images in Fig. 5 show that both and the custom filter set and the combination of the blocked 308 NBP & WG305 LWP filters adequately suppress the background emission. However, OH signal levels are significantly stronger with the custom filter set. An analysis of the OH intensity in several images with both filter sets, combined with the factor of 2.7 in intensifier gain, showed that OH signal levels were 4 to 5 times higher with the custom filter set. The superior transmission of the custom filter set allows regions of weak OH signal to be seen, and it makes the overall image sharper since there is less shot noise.

For the images taken through the piston-crown window, the liquid-phase portion of the fuel spray is also in the field of view (see Fig. 4). With the laser-sheet on the fuel-jet axis, the elastic scattering from the liquid phase fuel is very intense. The on- and off-line images in Fig. 6 show that despite the significant attenuation of the laser line by the filter sets, some elastic scattering comes through for both the custom (312 BP & 358 SWP) and combination (308 NBP & WG305) filter sets. By adding an additional WG305 LWP filter to either filter set, the elastic scattering could be virtually eliminated as demonstrated in Fig. 6 for the custom filter set. However, this was not necessary because the liquid-phase elastic-scatter signal is spatially separated from the OH PLIF signal as shown by a comparison of the on- and off-line images for the custom filter. Moreover, leaving the residual elastic-scatter signal in the OH PLIF images allows the location of the diffusion flame with respect to the liquid fuel to be seen.* Fig. 6 also shows the advantage of the custom filter set over the 308 NBP-&-WG305 combination in terms of OH signal strength, particularly in the upstream region where signals are weaker. Since it provides the best compromise between signal strength and low background noise, the custom filter set was used for the OH image sequences presented in the following figures.

RESULTS AND DISCUSSION

Because each view has advantages, OH PLIF images were acquired through both the piston-crown and cylinder-head windows. As shown in Figs. 4 and 6, the piston-crown window gives a full view of the fuel jet from the injector to the edge of the combustion bowl. In contrast, the cylinder-head window provides a view of the squish region as well as the outer part of the combustion bowl (the region beyond 27 mm from the injector). The cylinder-head window also allows the camera to be positioned closer to the fuel jet so higher resolution images can be obtained with about the same amount of light per pixel as the piston-crown window images.

The low-sooting fuel was used for the image sequences presented in the following subsections (Figs. 7 and 9-12), since its ignition, early soot formation and heat release rate have been shown to be virtually identical to those of a representative diesel fuel [23], as discussed in the Operating Conditions subsection. The pure TEOP fuel is used for one image pair (Fig. 8) because the reduced attenuation allows more detail to be seen. As with Figs. 5 and 6, the image intensity in all the remaining figures is displayed using a simple gray scale that goes from black to white as intensity increases minimum to maximum.

ON-AXIS TEMPORAL IMAGE SEQUENCE - PISTON-CROWN WINDOW

A temporal sequence of OH PLIF images taken through the piston-crown window is presented in Fig. 7. These images were acquired with the custom filter set, and as discussed in the previous section, strong elastic scatter from the liquid fuel is visible as well as the OH signal (see Fig. 6). In the first several images, the location of the injector tip is evident at the left edge along with a strong liquid-phase fuel signal from 5 of the 8 fuel jets. The gray curve at the right marks the edge of the combustion bowl (see Fig. 4), and the horizontal distance from the injector to the edge of the bowl is 49 mm. The laser sheet enters the field of view from the right along the axis of the fuel jet in the 3 o'clock position, as shown in Fig. 4. Although laser-sheet orientation, limited sheet width, and attenuation effects cause the liquid fuel dis-

* A 315 nm NBP filter which isolates the (1,1) band was also tried, but signals were much weaker than with the 308 NBP filter which collects light from the (0,0) band.

** 312 nm was selected as the center wavelength so that the peak transmission was near the stronger lines in the 308-320 nm emission band [31].

* Although these filter sets allow some liquid-fuel signal in the images, they adequately reject the weaker elastic scatter signal from the soot as was verified by obtaining on- and off-line images (similar to those in Fig. 6) for all crank angles presented.

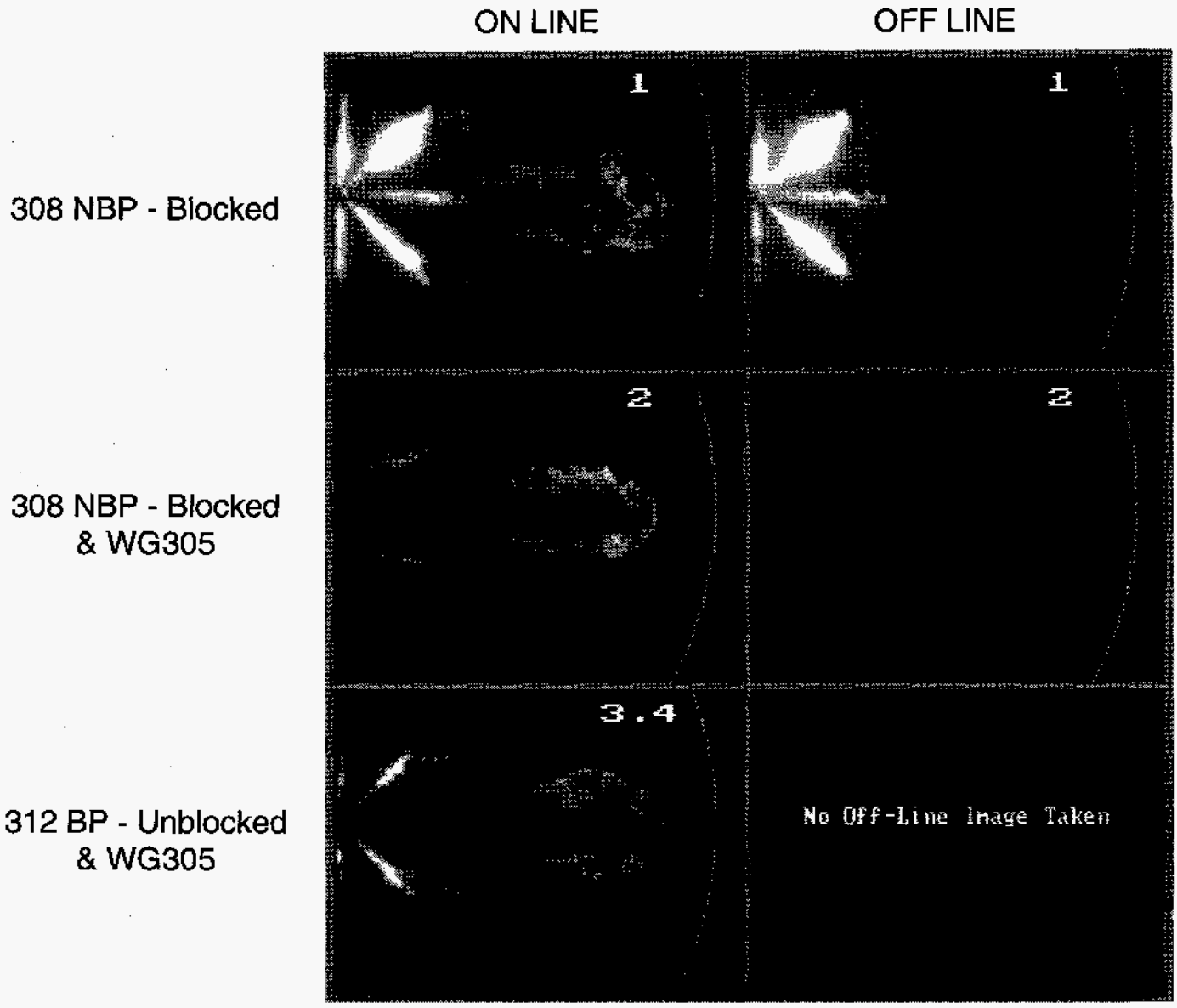

Figure 6. The effect of various filter combinations on the OH PLIF images obtained through the piston-crown window at 6.5° ASI with the laser sheet on the fuel-jet axis. On and off-line images are shown for the first two filter combinations. The number at the upper right of each image indicates the camera gain relative to that used for the custom filter set. The rectangular field of view is 54 mm by 41 mm, and the gray curve shown in the right of each image indicates the edge of the combustion bowl (limit of the field of view through this window, see Figs. 1 and 4).

tribution among the fuel jets to appear unequal, a previous study [25] has shown that all eight jets are very symmetric throughout the combustion event.

The sequence begins at 5.0° ASI. This first image shows a strong elastic scatter signal from the liquid-phase fuel, but there is no detectable OH since the on- and off-line (not shown) images are indistinguishable. At this crank angle the premixed vapor-fuel/air region of the jet extends well out beyond the liquid phase as indicated by the dashed line in the figure. (The extent of the vapor fuel was determined by Rayleigh scatter and chemiluminescence imaging [2,23].) Despite the absence of OH signal, there is strong evidence that the premixed burn is well under way in the leading portion of the fuel jet, downstream of the visible liquid-fuel region. The apparent heat release rate curve in Fig. 2 shows that the premixed burn began at 4.0° ASI, and that significant heat release has occurred by 5.0° ASI. In addition, by 5.0° ASI, quantitative Rayleigh fuel vapor images show fuel breakdown in the premixed region of the jet and natural chemiluminescence images show significant emission [23].

We can only conclude that OH concentrations in the premixed burn are too low to be detected with OH PLIF. This should not be surprising since the quantitative Rayleigh fuel vapor images show that the equivalence ratio of the premixed burn at these conditions is mostly in the range of 2 to 4 [1,2,23], and the OH concentration drops rapidly as equivalence ratios become increasingly rich. As discussed in the Introduction, Lucht et al. [11] showed that both peak and post-combustion OH concentrations in a premixed flame decreased by about a factor of 100 as the equivalence ratio was

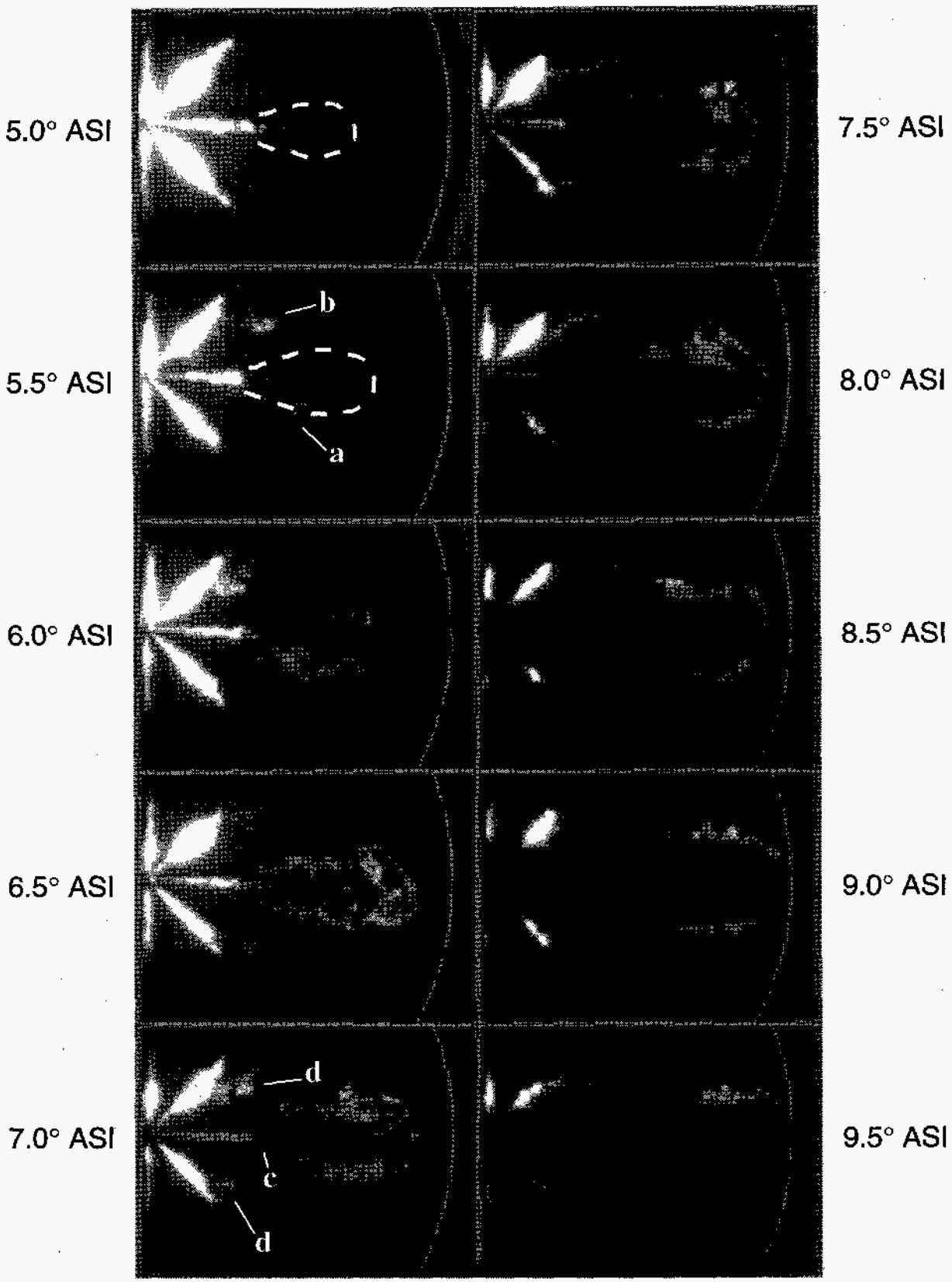

Figure 7. Temporal sequence of OH PLIF images obtained through the piston-crown window. For all images, the laser sheet was on the fuel-jet axis and the custom filter set (unblocked 312 nm bandpass and 358 nm SWP) was used. The crank angle degree after the start of injection (ASI) is given at the side of each image. The rectangular field of view is 54 mm by 41 mm, and the gray curve shown in the right of each image indicates the edge of the combustion bowl (limit of the field of view through this window, see Figs. 1 and 4). The labels "a", "b", "c", and "d" are explained in the text.

increased from 0.78 to 2.02. This is in general agreement with StanJan equilibrium calculations for diesel conditions which predict a decrease in OH by a factor of about 300 as the equivalence ratio is increased from 1 to 2 [33]. Equilibrium calculations indicate an even more severe drop in OH concentration for higher equivalence ratios, factors of 10^6 and 10^8 (relative to a stoichiometric mixture) for equivalence ratios of 3 and 4, respectively. These low OH concentrations are well below the detectability limits of any typical OH PLIF imaging system.

At 5.5° ASI, the first indication of OH is seen at the sides of the premixed combustion area. In the image presented, two regions of OH signal are visible. The dimmer region, labeled "a", is on the periphery of the premixed combustion zone (indicated by the dashed line) of fuel jet in the 3 o'clock position. The brighter spot of OH PLIF, labeled "b", is in a similar location relative to the periphery of the adjacent fuel jet. We believe this OH arises from the onset of diffusion combustion.

By 6.0° ASI, the PLIF image shows OH extending around a large fraction of the periphery of the premixed vapor-fuel/air region in the leading portion of the jet. Then, at 6.5° ASI, the leading portion of the reacting fuel jet is completely surrounded by a thin layer of OH. Through the rest of the sequence, OH is present around the periphery of the combusting jet. We believe that the OH signal in these images arises from a diffusion flame around the jet periphery. Eventually, the fuel-rich premixed burn progresses to the point where temperatures and radical concentrations are sufficiently high for a diffusion flame to develop at the interface between the partially reacted premixed portion of the fuel-jet (which contains significant excess fuel) and the surrounding air. As discussed in the Introduction, OH super-equilibrium concentrations in diffusion flames are quite high and should easily be visible with PLIF imaging. Also, the rate at which these flame-zone super-equilibrium concentrations are reduced to equilibrium levels is quite high at diesel conditions so that the detectable OH concentrations are confined to a narrow region about the flame front itself. The nature of the diffusion flame and the ability of OH PLIF to image it, will be discussed in detail in the Discussion subsection (see also the Introduction and Refs. [12,13 & 17]).

Attenuation effects on the OH signal are evident beginning with the 7.0° image. In this image, OH exists around the periphery of the 3 o'clock fuel jet in a pattern similar to the 6.5° ASI image except that the signal is weak or nonexistent in the upstream regions of the reacting portion of the jet (the area labeled "c"). However, OH must be present in this region since a strong OH signal is clearly visible along the sides of the two adjacent fuel jets in this same upstream region (areas labeled "d"). Attenuation of the laser sheet is clearly indicated. As it traverses the length of the 3 o'clock fuel jet, the laser is attenuated by absorption and/or scattering by OH, PAH and soot, so that little energy is left to pump the fluorescence in the upstream region. In contrast, the OH signal in the upstream regions of the two adjacent jets is much brighter since they are side illuminated and the laser sheet still has its full power. The attenuation of the laser sheet is also evident in the reduced elastic scatter signal from the liquid fuel region of the 3 o'clock jet.*

Attenuation becomes progressively worse through the rest of the sequence presented (7.0 to 9.5 ASI). The effects are seen first in the upstream portion because of the longer path length over which the laser power is attenuated. As soot and PAH concentrations increase further with time, the effective penetration length of the laser is progressively decreased. In addition, there can be attenuation of the signal from the plane of the laser sheet to the camera, although for most cases this is of lesser importance than the laser attenuation because the path length from center to edge of the jet is much shorter than the laser path along the jet axis.

At these later crank angles (>7.0° ASI), the OH appears to remain in a relatively thin region around the periphery as it was at the earlier crank angles when there was no apparent attenuation. However, severe attenuation could cause a similar apparent distribution pattern as has been demonstrated for soot imaging by Dec et al. [26]. In order to estimate the effect of attenuation on the OH images, we used the "noise" emission from PAH fluorescence and LII as a marker. By changing the optical filters, PAH/LII emission could be imaged along with the OH signal, similar to the first image in Fig. 5. As seen in Fig. 5, PAH/LII emission exists throughout the central region of the jet, so it shows how far inward from the leading edge and/or sides of the jet a signal can be obtained. The PAH/LII signal indicated that up through 8.0° ASI, attenuation has a minimal effect on the OH signal at the leading edge and along the sides of the jet, extending upstream to almost the same point where the OH signal becomes weak and spatially intermittent. By 8.5° ASI, attenuation is worse, and the OH signal is valid only at the leading edge and for about the first 10 mm back along the sides (about half to two-thirds the distance from the leading edge to the upstream extent of the OH signal).

Beyond 8.5° ASI, it was more difficult to assess the effects of attenuation on the images in Fig. 7 (and those to be presented in the next subsection in Fig. 9). The PAH/LII images indicated that the laser penetrates inward slightly from the periphery at the leading edge, so we believe that the images in Fig. 7 are accurate in showing the OH distribution as a thin zone at the front of the jet. (Note that the lack of OH signal at the tip of the jet at 9.0° and 9.5° ASI is caused by the jet penetrating beyond the field of view, not attenuation.) Interpretation of the signals back along the side of the jet at these crank angles is not as straightforward, and will be discussed further in the next subsection.

Images were not acquired at crank angles later than 9.5° ASI since attenuation was severe. We attempted to alleviate this problem by using the pure TEOP fuel; however, the reduction in attenuation was minimal, and the images are not

* Prior to 7.0° ASI there was virtually no attenuation. In the 6.5° ASI image (Fig. 7), there is a reasonable OH signal in the upstream region, and the intensity of the elastic-scatter signal from the liquid fuel is almost as strong as at earlier crankangles. Also, there is little attenuation of the OH signal as it travels from the plane of the laser to the camera, as will be evident from the images presented in Fig. 12.

presented. For future studies, changing the orientation of the laser sheet so that the jet is side illuminated would mitigate the attenuation problem on one side of the fuel jet. Since the jet is symmetric, this should allow the OH distribution and hence diffusion flame structure to be examined for a greater portion of the combustion event.

Although attenuation has some effects on the images beyond 7.0° ASI, the general nature of the diffusion-flame zone can still be seen for several crank angles, particularly toward the leading edge. For the most part, it remains confined to a relatively thin region around the extreme periphery of the fuel jet as the jet penetrates across the combustion chamber. Also, the OH signal from the upstream region of the two fuel jets adjacent to the 3 o'clock jet shows that the upstream end of the diffusion flame remains back along the sides of the tip of the liquid-phase fuel penetration. This is particularly evident in the 7.0°, 7.5°, and 8.0° ASI images in Fig. 7.

To better show the details of the diffusion flame attachment at the upstream end of the combusting region, Fig. 8 presents on- and off-line images using the pure TEOP fuel. These images were acquired at 5.0° ASI at which time the diffusion flame development is equivalent to that at 6.5° ASI for the low-sooting fuel (Fig. 7) due to the shorter ignition delay with the higher-cetane-number pure TEOP fuel. The pure TEOP results in somewhat less laser-sheet attenuation than the low-sooting fuel so the OH in the upstream region is better illuminated than it is in the 6.5° ASI image in Fig. 7. However, we had not received the custom filters at the time this data set was taken so the images were acquired using the blocked 308 NBP and WG305 LWP filter set, and image quality is not as good. Despite the lower signal strength, the better illumination improves our view of the upstream attachment of the diffusion flame. A comparison of the two images in Fig. 8 shows that the OH extends upstream of the tip of the liquid penetration, and that it comes in close to the liquid-fuel region along the jet axis.

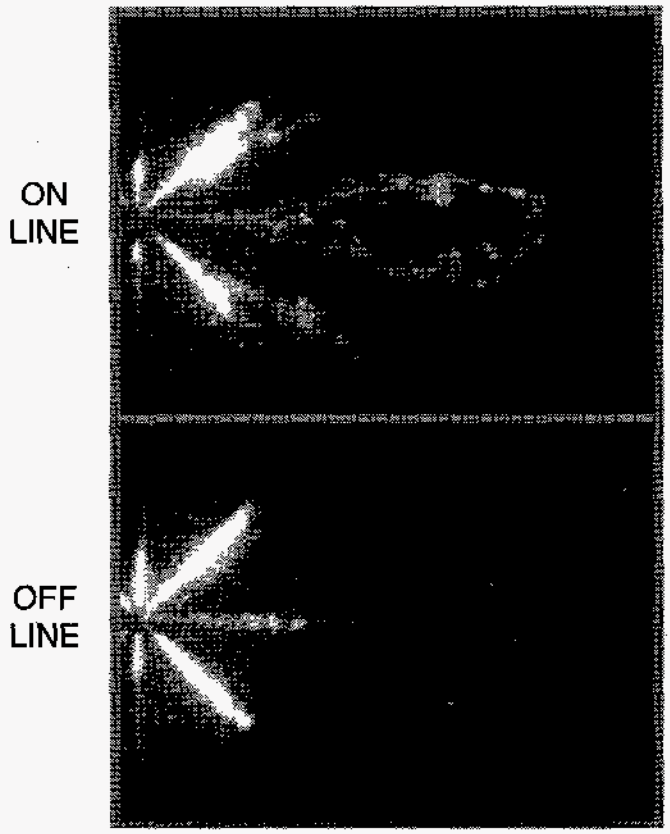

Figure 8. Details of the upstream extent of the diffusion flame. Shown are on- and off-line images through the piston-crown window at 5.0° ASI for the pure TEOP fuel. The filter set was a combination of a 308 narrow-bandpass filter and a WG305 Schott glass long-wave pass.

ON-AXIS TEMPORAL IMAGE SEQUENCE - CYLINDER-HEAD WINDOW

Figure 9 presents a temporal sequence of OH PLIF images obtained through the cylinder-head window for the same crank angles (5.0° to 9.5° ASI) as the sequence in Fig. 7. Also like Fig. 7, the laser sheet was on the fuel jet axis and the custom filter set was used. The field of view measures 30 x 22 mm, and the gray curve at the left shows the outline of cylinder-head window (see Fig. 4). The left edge of the window is 27 mm along the nominal fuel-jet axis (26 mm horizontally) from the injector, so only the leading portion of the reacting fuel jet is seen.

The development of the OH distribution shown in this sequence follows the same main steps discussed above for Fig. 7. However, the images have a higher resolution that shows more detail of the diffusion flame structure since the camera could be positioned closer to the fuel jet (see Fig. 1). At 5.0° ASI, the leading portion of the jet is within the view of the cylinder-head window, but there is no detectable OH signal from the fuel-rich premixed burn. Then, at 5.5° ASI, the first OH is seen at the sides of the premixed region at the extreme left edge of the field of view. This location of the first OH is in agreement with Fig. 7, and it indicates that the diffusion flame first develops toward the upstream end of the premixed vapor-fuel/air region at the periphery of the jet. By 6.0° ASI, the diffusion flame zone extends around a good deal of the leading portion of the fuel jet, and by 6.5° ASI the entire vapor-fuel region is encircled by a diffusion flame. This diffusion flame pattern then persists through the rest of the sequence.

In the image sequence in Fig. 9, little attenuation is evident up through the 8.0° ASI image. The upstream regions where attenuation was noted from 7.0° to 8.0° ASI in Fig. 7 are not within the field of view in Fig. 9. Beginning with the 8.5° ASI image, attenuation is indicated as the signal becomes nonexistent in parts of the upstream portion of the field of view. As discussed in the previous subsection, even though some OH signal is present in this upstream region (as along the bottom side of the jet in the image presented) attenuation may be limiting its inward extent, and the OH distribution in the image is only valid in the front half (first 10 mm from the leading edge) of the jet at 8.5° ASI.

At 9.0° and 9.5° ASI, attenuation has an increasing effect. As discussed in the previous subsection, PAH/LII signals indicated that the apparent OH distribution is probably accurate at the leading edge, but that there are significant attenuation affects along the sides of the jet that vary from cycle

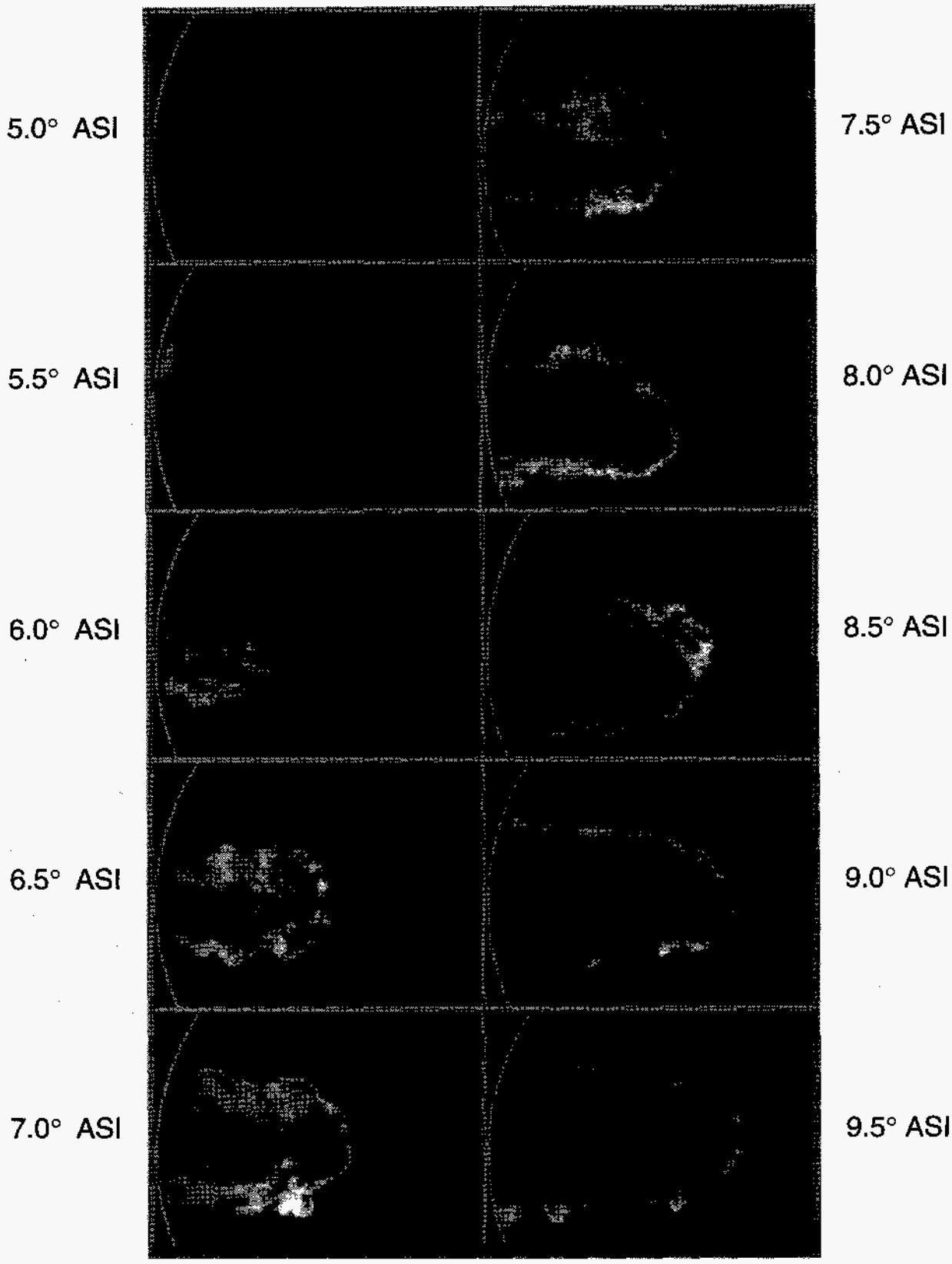

Figure 9. Temporal sequence of OH PLIF images obtained through the cylinder-head window. For all images, the laser sheet was on the fuel-jet axis and the custom filter set (unblocked 312 nm bandpass and 358 nm SWP) was used. The crank angle degree after the start of injection (ASI) is given at the side of each image. The rectangular imaged area corresponds to 30 mm by 22 mm, and the gray curve shown in the left of each image indicates the limit of the field of view through this window (see Fig. 4).

to cycle. Still, some indications of the OH distribution along the sides can be drawn with careful examination of the individual images. There are some areas where attenuation is clearly affecting the apparent OH distribution, such as the upstream part of the top side of the jet in the 9.0° ASI image. Here the inside edge of the OH distribution appears as a straight line because somewhere prior to reaching this part of the jet, the central part of the laser sheet has been severely attenuated. In other areas attenuation appears not to be affecting OH distribution, such as downstream part of the top side of the jet at 9.0° ASI. Here we see the OH as a thin layer around the outside of a small bulge in the jet. Because the laser is propagating from the right to the left and we see good signal from the left side, we can conclude that laser attenuation does not affect this region. Although signal attenuation between the plane of the laser and the surface of the jet could have an effect, near the edge of the jet the path is short, so it is unlikely to cause the OH signal to go from strong levels to being undetectable less than a millimeter away. Accordingly, the OH distribution in this area is probably accurate. Similar effects can be found in the 9.5° ASI image and in images from other cycles (not shown) obtained at these crankangles. Overall, these images give strong indications that up through 9.5° ASI, the diffusion flame remains as a fairly thin reaction zone around the jet periphery, as it appeared at earlier crankangles when attenuation effects were minimal.

It should be noted that as the diffusion flame is developing, there is considerable cycle-to-cycle variation in the OH distribution. At 5.5° ASI, when OH is present within the field of view, it is in the upstream region as shown in Fig. 9; however, its exact position varies, and it is not visible in many cycles. By 6.0° ASI, OH is always seen at the periphery of the leading portion of the fuel jet. The image in Fig. 9 is typical, but in some cycles only a small fraction of the periphery shows a diffusion flame, and in others the flame encompasses nearly the entire jet within the field of view. In virtually all cycles, the diffusion flame is well established by 6.5° ASI, and it completely surrounds the periphery of the fuel jet.

Although there is less gross variation in the OH distribution from cycle-to-cycle after 6.5° ASI, cycle-to-cycle variation in the detailed diffusion flame structure is still significant. Figure 10 presents an example of typical cycle-to-cycle variation after the diffusion flame is established. Shown are OH PLIF images of the diffusion flame for six different cycles at 7.0° ASI. The three images on the left are more

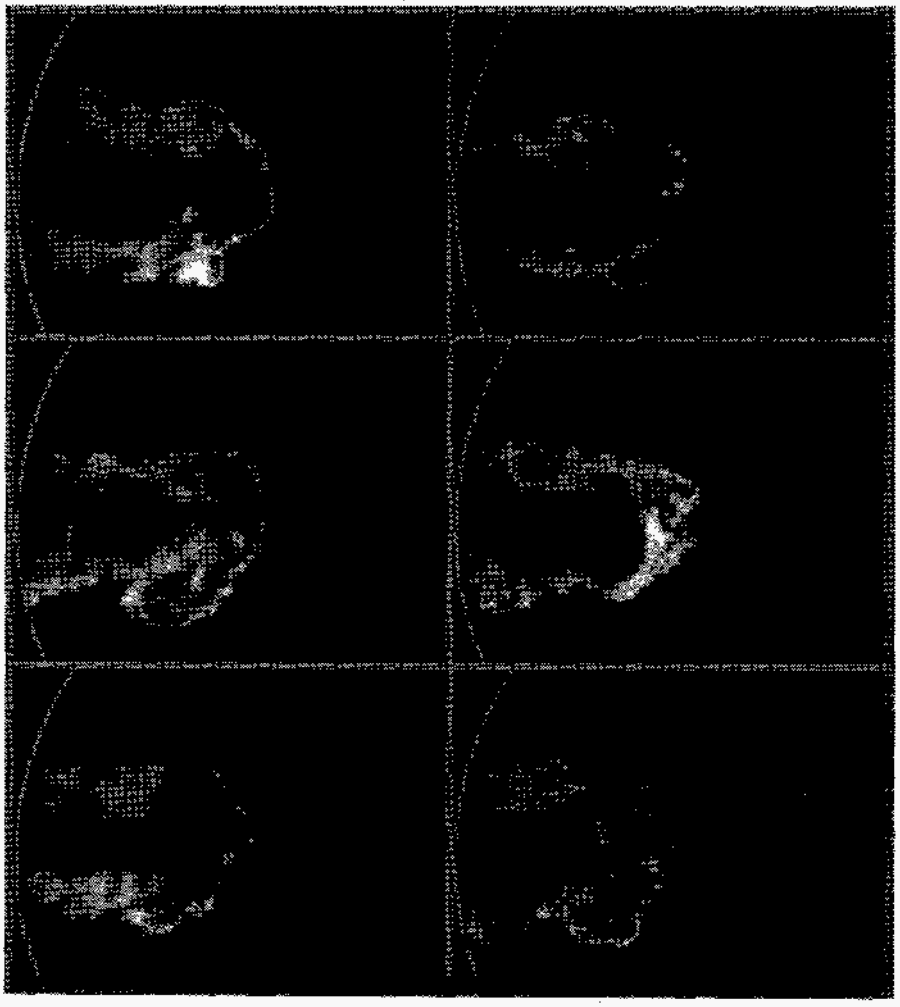

Figure 10. Cycle-to-cycle variation in OH PLIF images at 7.0° ASI. The images were obtained through the cylinder-head window, the laser sheet was on the fuel-jet axis, and the custom filter set (unblocked 312 nm bandpass and 358 nm SWP) was used. The rectangular imaged area corresponds to 30 mm by 22 mm, and the gray curve shown in the left of each image indicates the limit of the field of view through this window (Fig. 4).

typical cycles, while the three on the right are more extreme cases. The overall penetration of the fuel jet and the presence of OH only at the periphery is similar in all cycles, but the detailed structure varies.

HORIZONTAL LASER-SHEET IMAGE SEQUENCES

OH PLIF images were also acquired through the cylinder-head window with the laser sheet oriented horizontally as shown in Fig. 4. Figure 11 presents a temporal sequence of these image with the laser in the plane 9 mm below the cylinder head. At this elevation, the laser sheet is near the vertical center of the leading edge of the jet. Because the angle between the fuel-jet axis and the laser sheet is only 14°, and the jet is imaged over only a short length, this image sequence appears quite similar to the on-axis sequence presented in Fig. 9.

By traversing the laser sheet vertically, the horizontal laser sheet can be used to partially map out the OH distribution in the third dimension. Figure 12 shows a sequence of images at 6.5° ASI taken from 8 mm to 14 mm below the cylinder head at 2 mm intervals. Unfortunately, the geometry of the laser-entrance window did not permit images at elevations above 8 mm so the top of the reacting fuel jet could not be imaged. At 8 mm, the laser sheet is still near the center of the fuel jet, and the image is similar to the 9 mm image in Fig. 11 with the OH signal mainly at the jet periphery. At 10 mm, the flame zone still appears at the jet periphery except at the left edge of the field of view. Here the OH signal extends across the jet because at this elevation the horizontal laser sheet exits the bottom of the fuel jet directly below the left edge of the cylinder-head window. At 12 mm, the exit point of the laser sheet is shifted farther to the right, and the diffusion flame appears as a somewhat distorted circle. In this image, the diffusion flame appears wide at the left edge because the sheet is exiting the jet at a shallow 14° angle. The flame zone appears narrow at the leading edge because the flame front is more normal to the laser sheet. At 14 mm, the laser sheet is nearly tangential to the bottom of the jet, and the OH is present over most of the imaged portion of the fuel jet, although a small region of no signal and thin flame zone are still evident at the right.

DISCUSSION

Diffusion Flame Structure - Like the full-jet images obtained through the piston-crown window (Figs. 7 and 8), the high-resolution images obtained through the cylinder-head window (Figs. 9 - 12) show that the diffusion flame is confined to the jet periphery with no signal evident in the central region of the jet. However, the high-resolution images also reveal many smaller-scale details of the early diffusion-flame structure in diesel combustion.

In interpreting these images, care must be taken because they are two-dimensional (2-D) slices through a turbulent 3-D structure. When the flame front is normal to the plane of the laser, it will appear as a thin sheet, and image interpretation is straightforward as long as the flame fronts are not too close together. Alternatively, when the flame is at an angle to the plane of the laser, it will appear thicker, and in the extreme

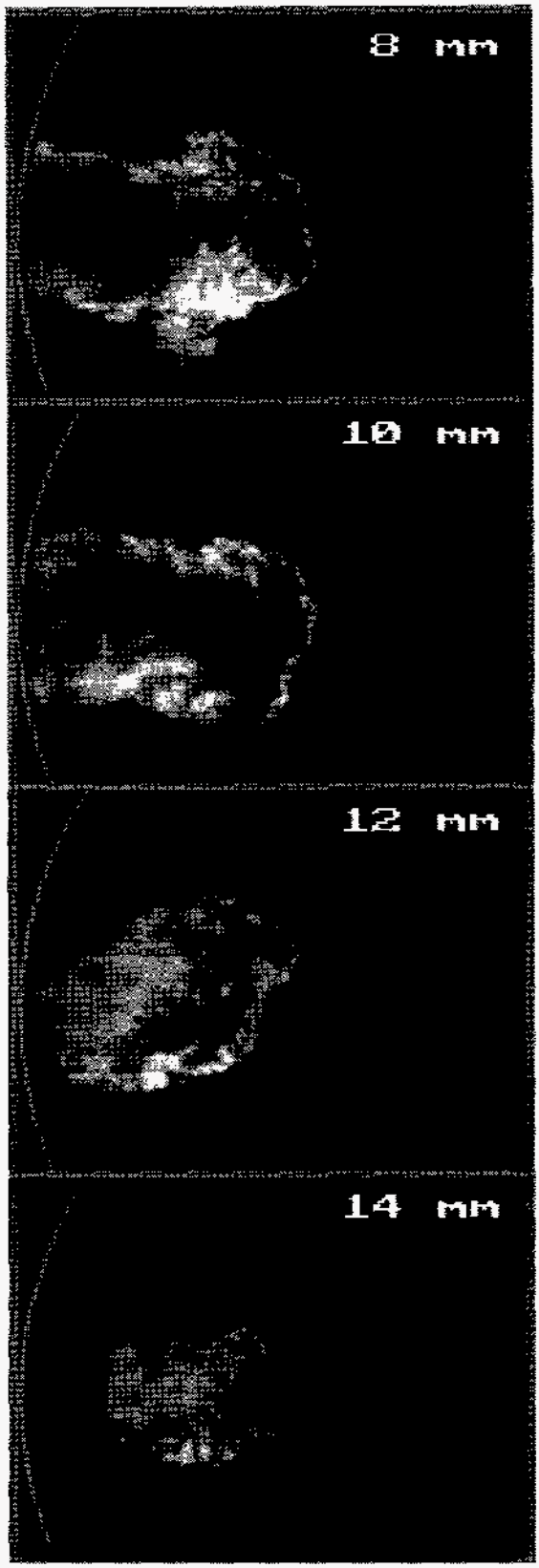

Figure 12 Vertical sequence of OH PLIF images at 6.5° ASI, obtained through the cylinder-head window with the horizontal laser sheet (see Fig. 4) and the custom filter set. The distance below the cylinder head is given in the upper right of each image. The rectangular imaged area corresponds to 30 mm by 22 mm, and the gray curve shown in the left of each image indicates the limit of the field of view through this window.

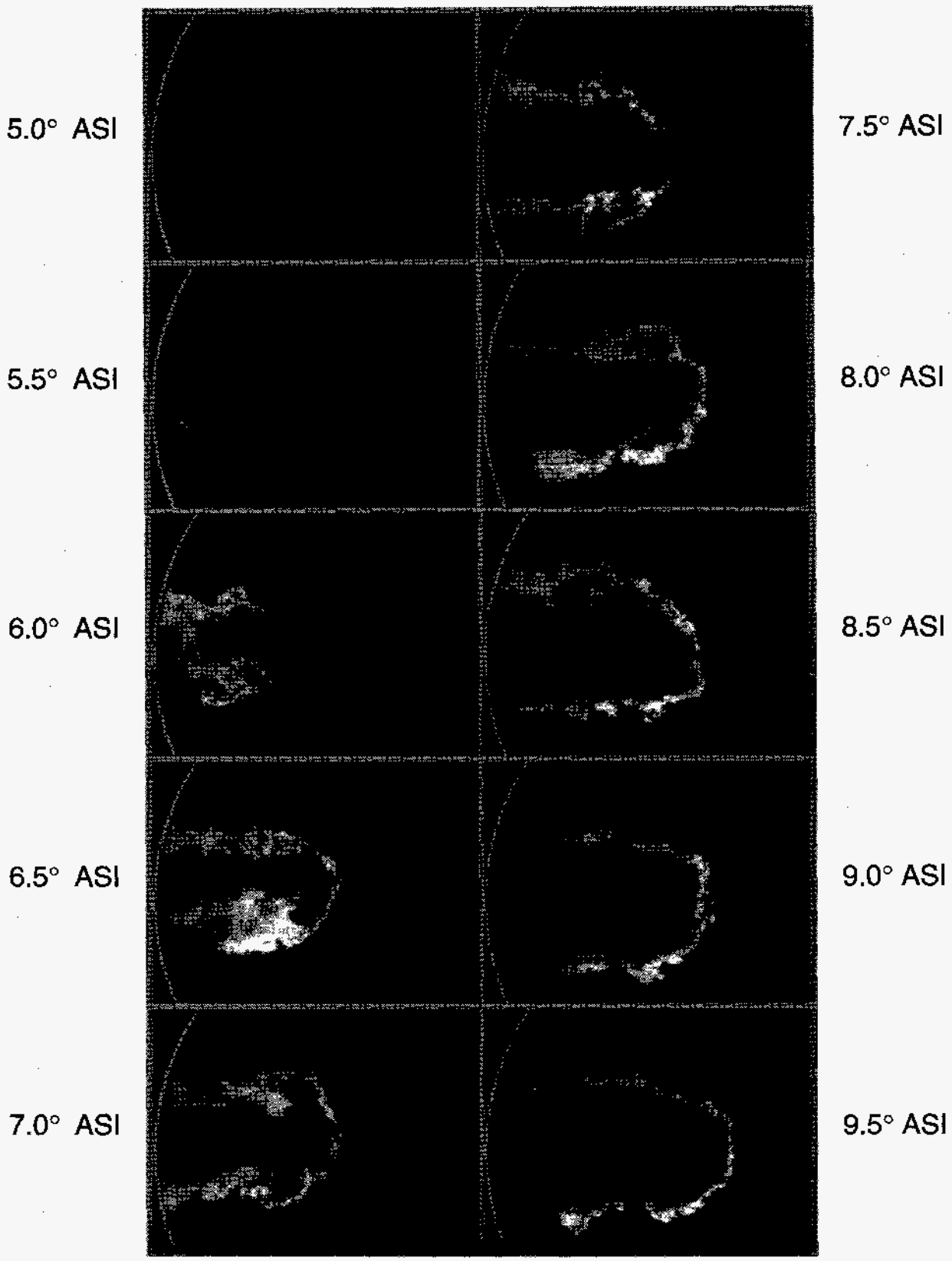

Figure 11. Temporal sequence of OH PLIF images obtained through the cylinder-head window with the horizontal laser sheet in the plane 9 mm below the cylinder head (see Fig. 4) using the custom filter set. The crank angle degree after the start of injection (ASI) is given at the side of each image. The rectangular imaged area corresponds to 30 mm by 22 mm, and the gray curve shown in the left of each image indicates the limit of the field of view through this window.

case, when a curved surface of the flame is tangential to the laser sheet, it will appear as a broad region of OH signal. As a result, regions of distributed OH signal can be difficult to interpret. They could result from any one or a combination of the following: multiple individual flame fronts all normal to the laser sheet but too close together to be resolved by the imaging system, sections of the flame sheet that are at an angle or tangential to the laser sheet, or a distributed reaction zone ("thick flame").

Although subject to these limitations, the 2-D images provide much information on the details of the diffusion flame structure. Over large portions of the jet surface, the diffusion flame appears as a very thin sheet. In some cases, this diffusion flame sheet is relatively smooth such as at the leading edge of the 7.0° ASI image in Fig. 9, and in others significant wrinkling by turbulence is noted such as the upper-right portion of the fuel jet in the 7.5° and 8.0° ASI images in Fig. 9. Even in regions where the OH distribution is generally broader, thin flame sheets can sometimes be seen between the regions of broader OH distribution, as evident along the bottom of the 6.5° and 7.0° ASI jets in Fig. 9. Examination of these thin-sheet areas under high magnification shows that these flame fronts measure only about 2 pixels or 120 μm thick in regions where they are fairly smooth. Since various factors can limit the actual optical resolution of an intensified video camera system to be somewhat less than a single pixel [34], this number represents an upper limit to the diffusion flame thickness. The actual diffusion flame may be significantly thinner than this and may vary from place to place around the jet and from cycle to cycle. Also, the flame sheet must be nearly perpendicular to the image plane since the laser-sheet thickness is about 250 μm.

We can draw two significant conclusions from this measurement. First, the basic nature of the diesel diffusion flame is that of a very thin sheet, similar to those observed in laminar diffusion flame burners. Second, as hypothesized above, the high rate at which flame-front OH-super-equilibrium concentrations are reduced to equilibrium levels at diesel pressures, combined with the rapid drop in OH equilibrium concentration outside of a diffusion flame, confines high OH concentrations to a very narrow region around the diffusion flame.*

This latter point has important ramifications for laser-imaging diagnostics for diesel combustion. Based on atmospheric-pressure burner and spark-ignition engine experiments, PLIF of OH was generally not considered to be a particularly good diagnostic for flame zone imaging, because high OH concentrations persisted in the post-combustion gases making flame zone identification difficult. This is clearly not the case for diffusion flames at diesel-engine conditions. The images presented here show that the high OH concentrations closely mark the diffusion flame for the reasons explained above. Accordingly, for diffusion flame imaging in diesel engines, OH is an excellent diagnostic, and there is no need to use alternative techniques that are often more difficult to implement such as CH radical imaging. However, for studying the premixed combustion, alternative diagnostics are needed since OH is not present in detectable concentrations.

Although the OH PLIF images show a thin diffusion flame in many regions, the flame is particularly thin and smooth at the leading edge of the jet (for example, the three left hand images in Fig. 10). This occurs because, from a flame reference frame, the center of the leading edge of the jet is the stagnation point of an opposed-flow diffusion flame between the jet flow and the relative flow of surrounding air (resulting from jet penetration). Once the jet flow reaches the stagnation point, it must turn and flow radially outward. As a result, shear rates and turbulence production are low at the leading edge.

In other parts of the jet (particularly along the sides) the OH signal is more broadly distributed. Image interpretation in these regions is difficult for the reasons discussed at the beginning of this subsection, but some inferences can be drawn.

The images show fairly strong correlation between the regions of broader OH distribution and the existence of larger-scale turbulent structures. This is particularly evident in the 7.5° ASI image in Fig. 9 which shows a broad OH distribution only along the sides of the jet just upstream of the leading edge where the outline of the fuel jet indicates the development of a large roll-up vortex. Also, in the 6.5° and 7.0° ASI images in Fig. 9 (and in many of the images in Fig. 10) where broad OH regions are seen along the sides of the jet, the outline of the jet indicates the presence of larger turbulent structures, as would be expected because of the higher shear along the sides of the jet. Regions of larger-scale turbulent vortices and generally higher turbulence levels would cause the diffusion flame to roll or fold up placing multiple flame zones in close proximity. In addition, because turbulence is 3-dimensional, many sections of these convoluted flames sheets would intersect the laser sheet at an angle (or even be tangential) making them appear wider. The combination of these two effects could cause the OH distribution in the images to appear broad, even though locally the diffusion flame remains thin.

This explanation for the regions of broad OH distribution is supported by the data in several ways. First, the correlation of the broad OH regions with the presence of increased turbulence provides strong circumstantial evidence as discussed above. Second, the basic nature of the diesel diffusion flame appears to be that of a thin sheet. This is evident in regions where a smooth outline of the jet indicates lower turbulence (as discussed previously), and also in higher turbulence regions, where short sections of very thin flames are visible between regions of broad OH distribution. Examples of this latter effect may be seen along the bottom side of jets in the 6.5° and 7.0° ASI images in Fig. 9 (see also Fig. 10). Finally, within the broader OH distribution zones there are often small regions of higher intensity that have a thin filament-like structure, indicating thin flame sheets that are not fully resolved. For these reasons, we believe that the broad

* Removal of OH by soot oxidation may also contribute to the narrow OH distribution, but this effect is limited to the fuel side so it cannot by itself explain the OH distributions observed here.

OH regions are caused by a highly convoluted thin diffusion-flame sheet, although the alternative explanation of a "thick flame" cannot be ruled out.

Regardless of the nature of the diffusion flame itself, the thicker OH distribution in some parts of the jet periphery indicates that turbulence distributes the region of diffusion combustion inward somewhat from the extreme periphery of the jet. However, a large portion of the central part of the jet remains separate from the diffusion flame process.

Relationship of the Diffusion Flame to other Combustion Events - The OH images sequences in Figs. 7 and 9 show that the first diffusion combustion is just starting in some cycles at 5.5° ASI, or 1.5° after the first indicated heat release. Then, within the next crank angle degree (140 μs) diffusion combustion develops around the rest of the periphery of the downstream portion of the fuel jet.* Thus, diffusion combustion has just been established around the jet periphery at 6.5° ASI which is approximately at the center of the premixed burn spike of the heat release rate curve (Fig. 2). This finding is in excellent agreement with an earlier study of the soot formation [23].

In this earlier work, which was conducted in this same engine at the same operating condition, Dec and Espey [23] investigated the onset of soot formation using simultaneous LII and elastic-scatter imaging. They found that the flame started to become luminous and small soot particles formed throughout the cross section of the downstream portion of the fuel jet beginning at 5.5° - 6.0° ASI. Then suddenly, at 6.5° ASI, much larger soot particles formed around the fuel-jet periphery. They deduced that these larger soot particles at the jet surface must arise from the initial diffusion flame, while the small particles were produced by the fuel-rich premixed burn. Although the large-soot-particle region did become thicker as time progressed, they remained generally confined to the peripheral region of the jet. The central region of the jet contained only small soot particles for the rest of the observed sequence.

The OH PLIF data from the current study confirms the timing of the onset of diffusion combustion proposed in the earlier work. In addition, the coincidence in both timing and spatial distribution (around the jet periphery) between the initial diffusion flame and the first large soot particles strongly supports the diffusion flame being the source of the larger soot particles. After their initial development, both the diffusion flame and the large soot particles remain in the peripheral regions of the jet; however, the large particles appear to spread inward somewhat more than does the diffusion flame itself, as might be expected from turbulent transport.

Although OH concentrations in the fuel-rich premixed flame zones are too low to be detected, the current diffusion flame images combined with previous soot distribution data suggest that a fuel-rich premixed flame (spatially separated from the diffusion flame) may exist during the mixing-controlled burn. The OH images show the diffusion flame at the jet periphery and give no indication of it moving inward up to the time when soot obscures the images. This suggests that the diffusion flame remains at the jet periphery during the rest of the injection event. Previous studies [25,35-37] have shown small soot particles throughout the cross section of the upstream portion of the vapor-phase region of the fuel jet up until the end of injection. Since soot formation requires temperatures above those of the in-cylinder air [38], if the diffusion flame remains at the jet periphery, a fuel-rich premixed flame in the upstream part of the vapor-phase region of the jet appears to be the only alternative source for these soot particles. This is in agreement with fuel/air mixture measurements (based on Rayleigh scattering) [1,2] that show the fuel at this axial location in the jet to be premixed with air to an equivalence ratio of about 4, a rich but combustible mixture under diesel conditions.

Finally, the understanding of the diesel diffusion flame provided by these OH PLIF images provides insight into the probable location of thermal NO production in the combusting diesel fuel jet. Although NO can be produced by other pathways such as the "prompt" mechanism, the Zeldovich or "thermal" mechanism is one of the most important pathways for diesel conditions. Production of thermal NO requires both high temperatures and the presence of oxygen. Since fuel-vapor concentration measurements [1,2] have shown that the premixed combustion is fuel-rich, the only area where these two criteria are met is on the air side of the diffusion flame. Accordingly, while the diffusion flame location remains as described above, high NO production rates by the thermal mechanism can occur only around the jet periphery on the lean side of the diffusion flame. However, the actual distribution of NO may be different, because the relatively slow rate of thermal NO production allows time for fluid mechanics to transport gases from these regions of high production to other parts of the jet, and because NO can be formed by other mechanisms.

SUMMARY AND CONCLUSIONS

Planar laser-induced fluorescence (PLIF) of the OH radical has been demonstrated in a DI diesel engine, and the technique has been used to map out the structure of the early diffusion flame. The measurements were made in a single-cylinder optically accessible DI diesel engine derived from a Cummins N14 production engine, at a medium speed (1200 rpm) operating condition. The OH PLIF was excited in the (1,0) band of the A→X transition at 284.01 nm using a Nd:YAG-based laser system, while the fluorescent emission from both the (0,0) and (1,1) bands (308-320 nm) was imaged with an intensified video camera. This PLIF imaging scheme allowed elastically scattered laser light, PAH fluorescence, and laser-induced incandescence to be adequately rejected.

The study demonstrated that OH PLIF is an excellent diagnostic for studying diffusion flames in diesel engines. Signals are quite strong, and they are confined to a very narrow region about the flame sheet. This latter finding is contrary to findings in atmospheric flames. It occurs because the

* Note that the diffusion flame must start at multiple points around the jet periphery since 140 μs is not sufficient time for the diffusion flame to start at a single point and spread down the length of the jet.

three-body recombination reactions that reduce the high flame-front OH concentrations to equilibrium levels occur very rapidly at diesel pressures, and for diffusion flames, the OH equilibrium levels drop rapidly outside the flame zone. Together, these two factors produce a very sharp drop in OH concentration immediately outside the flame front.

No OH signal was detectable from the premixed combustion, which previous studies [1,2] have shown to be fuel rich. This is in agreement with burner experiments and calculations that show OH concentrations being 10^2 to 10^8 times lower than those in diffusion flames when mixtures are as rich as the premixed combustion in this diesel engine (equivalence ratios of 2 to 4).

The study produced the following results for the conditions studied:

1. There is no detectable OH signal from the initial fuel-rich premixed burn or from areas of suspected fuel-rich premixed combustion during the mixing-controlled burn, in agreement with the expected low OH concentrations.
2. The first indication of diffusion combustion begins about 1.5° crank angle before the center of the premixed burn spike in the apparent heat release rate curve.
3. The diffusion flame is fully established around the periphery of the downstream portion of the reacting fuel jet just before the center of the premixed burn spike (6.5° ASI).
4. This timing agrees well with the appearance of a class of larger soot particles around the jet periphery noted in a previous study [23], and attributed to the onset of diffusion combustion.
5. Once established, the diffusion flame encircles the downstream (vapor-phase) portion of the reacting fuel jet and extends back toward the injector to a point that is slightly upstream of the tip of the maximum liquid-phase fuel penetration.
6. Although affected by turbulence, the diffusion flame zone remains at the jet periphery throughout the imaged portion of the combustion event. By 8.5° ASI, soot was beginning to obscure the OH PLIF images, and images were not acquired after 9.5° ASI because of substantial attenuation. Attenuation effects could be mitigated by illuminating the fuel jet from the side in future studies.
7. In regions of lower apparent turbulence, the diffusion flame appears as a very thin sheet. The OH PLIF images (which have limited resolution) indicated a maximum flame thickness of 120 μm; the actual flame may be significantly thinner.
8. In regions of higher apparent turbulence, the OH signal is more broadly distributed, most probably because the diffusion flame sheet is highly convoluted.
9. The data suggest that the diffusion flame remains at the jet periphery, so it is not likely to be the source of the small soot particles that have been observed throughout the cross section of the upstream portion of the vapor-phase region of the fuel jet (beginning just downstream of the maximum liquid fuel penetration) [25,35-37]. A fuel-rich premixed flame standing slightly downstream of the maximum extent of the liquid fuel during the mixing-controlled burn appears to be the most likely source of these soot particles. Quantitative Rayleigh fuel images have indicated that the vapor-fuel and air mixture in this region is fuel rich but combustible under diesel conditions [1,2].
10. While the diffusion flame remains at the jet periphery, NO production by the Zeldovich (thermal) mechanism can only occur in a thin zone at the jet periphery on the air side of the diffusion flame, since this is the only location where temperatures are high and oxygen is present.

ACKNOWLEDGMENTS

The authors would like to thank Charlie Westbrook for guidance on expected OH concentrations in diffusion and fuel-rich premixed flames. They also thank Eldon Porter for maintaining the experimental apparatus and for help with the data acquisition. The authors would also like to express their gratitude to Patrick Flynn and Roy Primus of the Cummins Engine Co. for their support of this project.

This study was performed at the Combustion Research Facility, Sandia National Laboratories, Livermore, CA. The authors thank the Cummins Engine Company and the U.S. Department of Energy, Defense Programs Technology Transfer Initiative for supporting this work.

REFERENCES

1. Espey, C., Dec, J. E., Litzinger, T. A. and Santavicca, D. A., "Quantitative 2-D Fuel Vapor Concentration Imaging in a Firing D.I. Diesel Engine Using Planar Laser-Induced Rayleigh Scattering," *SAE Transactions*, Vol. 103, Sec. 4, pp. 1145-1160, paper no. 940682, 1994.
2. Espey, C., Dec, J. E., Litzinger, T. A. and Santavicca, D. A., "Quantitative Planar Rayleigh Scattering for Fuel Vapor Concentration Imaging in a Diesel Fuel Jet," submitted to *Combustion and Flame*, 1994.
3. Dyer, M. J. and Crosley, D. R., "Fluorescence Imaging for Flame Chemistry," in *Proceedings of the International Conference on Lasers '84*, p. 211, K. Corcoran, D. Sullivan, and W. Stwalley, eds. (STS, McLean, Va., 1985).
4. Allen, M.G. and Hanson, R. K., "Digital Imaging of Species Concentration Fields in Spray Flames," *Twenty-First Symposium (International) on Combustion*, The Combustion Institute, pp. 1755-1762, 1986.
5. Schefer, R. W., Namazian, M., and Kelley, J., "CH, OH and CH_4 Concentration Measurements in a Lifted Turbulent-Jet Diffusion Flame," *Twenty-Third Symposium (International) on Combustion*, The Combustion Institute, pp. 669-676, 1990.
6. Allen, M. G., Howe, R. D., and Hanson, R. K., "Digital Imaging of Reactions Zones in Hydrocarbon-Air Flames using Planar Laser-Induced Fluorescence of CH and C_2," *Optics Letters*, Vol. 11, No. 3, pp. 126-128, 1986.
7. Paul, P. H. and Dec, J. E., "Imaging of Reactions Zones in Hydrocarbon-Air Flames using Planar Laser-Induced Fluorescence of CH," *Optics Letters*, Vol. 19, No. 13, pp. 998-1000, 1994.

8. Dyer, M. J. and Crosley, D. R., "Two-Dimensional Imaging of OH Laser-Induced Fluorescence in a Flame," *Optics Letters*, Vol. 7, No. 8, pp. 382-384, 1982.
9. Kychakoff, G. Howe, R. D. Hanson, R. K., and McDaniel, J. C., "Quantitative Visualization of Combustion Species in a Plane," *Applied Optics*, Vol. 21, No. 18, pp. 3225-3227, 1982.
10. Sietzman, J. M., Üngüt, A., Paul, P. H., and Hanson, R. K., "Imaging and Characterization of OH Structures in a Turbulent Nonpremixed Flame," *Twenty-Third Symposium (International) on Combustion*, The Combustion Institute, pp. 637-644, 1990.
11. Lucht, R. P, Sweeney, D. W., and Laurendeau, N. M., "Laser-Saturated Fluorescence Measurements of OH in Atmospheric Pressure $CH_4/O_2/N_2$ Flames Under Sooting and Non-Sooting Conditions," *Combust. Sci. and Tech.*, Vol. 42, pp. 259-281, 1985.
12. Carter, D. C., King, G. B., and Laurendeau, N. M., "Laser-Induced Fluorescence Measurements of OH in Laminar $C_2H_6/O_2/N_2$ Flames at High Pressure," *Combust. Sci. and Tech.*, Vol. 71, pp. 263-273, 1990.
13. Barlow, R.S., Dibble, R.W., Chen, J.-Y., and Lucht, R.P., "Effect of Damköler Number on Superequilibrium OH Concentration in Turbulent Nonpremixed Jet Flames," *Combustion and Flame*, Vol. 82, pp. 235-251, 1990.
14. Millikan, R. C., "Non-Equilibrium Soot Formation in Premixed Flames," *J. Phys. Chem.*, Vol. 66, pp. 794-799, 1962.
15. Fenimore, C. P. and Jones, G. W., "Oxidation of Soot by Hydroxyl Radicals," *J. Phys. Chem.*, Vol. 71, pp. 593-597, 1967.
16. Puri, R., Santoro, R. J. and Smyth, K. C., "The Oxidation of Soot and Carbon in Hydrocarbon Diffusion Flames," *Combustion and Flame*, Vol. 97, pp. 125-144, 1994.
17. Allen, M. G., McManus, K. R., and Sonnenfroh, D. M. and Paul, P. H., "Planar Laser-Induced-Fluorescence Imaging of OH and Hydrocarbon Fuel Fragments in High-Pressure Spray-Flame Combustion," *Applied Optics*, Vol. 34, No. 27, pp. 6287-6300, 1995.
18. Bui-Pham, M. and Seshadri, K., "Comparison Between Experimental Measurements and Numerical Calculations of the Structure of Heptane-Air Diffusion Flames," *Combust. Sci. and Tech.*, Vol. 79, pp. 293-310, 1991.
19. Felton, P. G., Mantzaras, J., Bomse, D. S., and Woodin, R. L., "Initial Two-Dimensional Laser-Induced Fluorescence Measurements of OH Radicals in an Internal Combustion Engine," SAE paper no. 881633, 1988.
20. Suntz, R., Becker, H., Monkhouse, P., and Wolfrum, J., "Two-Dimensional Visualization of the Flame Front in an Internal Combustion Engine by Laser-Induced Fluorescence of OH Radicals," *Applied Physics B*, Vol. 47, pp. 287-293, 1988.
21. Serpengüzel, Hahn, T. T. and Acker, W. P., "Single-Pulse Planar Laser-Induced Fluorescence Imaging of Hydroxyl Radical in a Spark Ignition Engine," SAE paper no. 93701.
22. Arnold, A., Dinkelacker, F., Heitzmann, T., Monkhouse, P., Schäfer, M., Sick, V. and Wolfrum, J., "DI Diesel Engine Combustion Visualized by Combined Laser Techniques," *Twenty-Fourth Symposium (International) on Combustion*, The Combustion Institute, pp. 1605-1612, 1992.
23. Dec, J. E. and Espey, C., "Ignition and Early Soot Formation in a D.I. Diesel Engine Using Multiple 2-D Imaging Diagnostics," SAE paper 950456, 1995.
24. zur Loye, A. O., Siebers, D. L., McKinley, T. L., Ng, H. K., and Primus, R. J., "Cycle-Resolved LDV Measurements in a Motored Diesel Engine and Comparison with k-e Model Predictions," *SAE Transactions*, Vol. 98, Sec. 3, pp. 1142-1158, paper no. 890618, 1989.
25. Espey, C. and Dec, J. E., "Diesel Engine Combustion Studies in a Newly Designed Optical-Access Engine Using High-Speed Visualization and 2-D Laser Imaging," *SAE Transactions*, Vol. 102, J. Fuels and Lubricants, Sec. 4, pp. 703-723, paper no. 930971, 1993.
26. Dec, J. E., zur Loye, A. O., and Siebers, D. L., "Soot Distribution in a D.I. Diesel Engine Using 2-D Laser-Induced Incandescence Imaging," *SAE Transactions*, Vol. 100, Sec. 3, pp. 277-288, paper no. 910224, 1991.
27. Won, Y.-H., Kamimoto, T., Kobayashi, H., and Kosaka, H, "2-D Soot Visualization in Unsteady Spray Flame by means of Laser Sheet Scattering Technique," *SAE Transactions*, Vol. 100, Sec. 3, pp. 265-276, paper no. 910223, 1991.
28. Won, Y.-H., Kamimoto, T., and Kosaka, H, "A Study on Soot Formation in Unsteady Spray Flames via 2-D Soot Imaging," *SAE Transactions*, Vol. 101, Sec. 4, pp. 89-100, paper no. 920114, 1992.
29. Heywood, J. B., Internal Combustion Engine Fundamentals, pp. 509-511, McGraw-Hill, 1988.
30. Espey, C. and Dec, J. E., "The Effect of TDC Temperature and Density on the Liquid-Phase Fuel Penetration in a D.I. Diesel Engine," SAE paper 952456, 1995.
31. Dieke, G. H. and Crosswhite, H. M., "The Ultraviolet Bands of OH Fundamental Data," *J. Quant. Spectrosc. Radiat. Transfer*, Vol. 2, pp. 97-199, 1962.
32. Berlman, I. B., Handbook of Fluorescence Spectra of Aromatic Molecules, Academic Press, 1971.
33. Personal communication with Charles K. Westbrook of Lawrence Livermore National Laboratory.
34. Paul, P. H., "The Application of Intensified Array Detectors to Quantitative Planar Laser-Induced Fluorescence Imaging," AIAA paper 91-2315, 27th Joint Propulsion Conference, Sacramento, CA, June, 1991.
35. Dec, J. E. and Espey, C., "Soot and Liquid-Phase Fuel Distributions in a Newly Designed Optically Accessible D.I. Diesel Engine," Presented at the 1993 Diesel Emission Reduction Workshop, LaJolla, CA, July 1993, Sandia Laboratories Report No. SAND93-8690C.
36. Dec, J. E., "Soot Distribution in a D.I. Diesel Engine Using 2-D Imaging of Laser-Induced Incandescence, Elastic Scattering, and Flame Luminosity," *SAE Transactions*, Vol. 101, Sec. 4, pp. 101-112, paper no. 920115, 1992

37. Kosaka, H., Nishigaki, T., and Kamimoto, T., "A Study on Soot Formation and Oxidation in an Unsteady Spray Flame via Laser-Induced Incandescence and Scattering Techniques," SAE paper 952451, 1995.
38. Wagner, H. Gg., "Soot Formation - An Overview," pp. 1-29, Particulate Carbon Formation During Combustion, D.C. Siegla and G.W. Smith editors, Plenum Press, New York, 1981.

DISCLAIMER